Crystallization in additive manufacturing of metallic glass

Ericsson, Anders

2021

Document Version:
Publisher's PDF, also known as Version of record

LUNDS UNIVERSITET

CRYSTALLIZATION IN ADDITIVE MANUFACTURING OF METALLIC GLASS

ANDERS ERICSSON

Solid Mechanics

Doctoral Thesis

Crystallization in additive manufacturing of metallic glass

Anders Ericsson

LUND
UNIVERSITY

Akademisk avhandling som för avläggande av teknologie doktorsexamen vid tekniska fakulteten vid Lunds universitet kommer att offentligen försvaras fredagen den 10 december 2021 kl 09.00 i sal E:C, E-huset, Ole Römers väg 3, Lund.
Fakultetsopponent: Prof. Dr.-Ing. Torsten Markus, University of Mannheim, Tyskland.

Academic thesis which by due permission of the Faculty of Engineering at Lund University, will be publicly defended on the 10th of December 2021 at 09.00 in room E:C in the E-building, Ole Römers väg 3, Lund, for the degree of Doctor of Philosophy in Engineering.
Faculty opponent: Prof. Dr.-Ing. Torsten Markus, University of Mannheim, Germany.

Organization	Document name
LUND UNIVERSITY Division of Solid Mechanics Lund University P.O. Box 118 SE-221 00 LUND, Sweden	DOCTORAL DISSERTATION
	Date of issue October 2021
	Sponsoring organization
Author(s) Anders Ericsson	

Title and subtitle

Crystallization in additive manufacturing of metallic glass

Abstract

Metallic glasses are non-crystalline metals that are obtained by rapid cooling of the melt to bypass crystallization. The amorphous atomic structure show enhanced properties relative to the crystalline counterpart. For example, enhanced mechanical properties, improved corrosion resistance, as well as excellent soft magnetic properties. The unique properties of metallic glasses make them promising for a wide range of applications, e.g. spring materials, structural components, electrical motors, and biomedical implants. One drawback is the cooling rate required for glass formation, which limits the thickness of cast components to only a few millimeters. As a solution, additive manufacturing (AM) shows promising potential to produce large-scale metallic glass components. In AM, the solidification process is short and confined to a small volume that is repetitively added. Despite the high heating and cooling rates in AM, control of crystallization is still an issue and a complete understanding of the interplay between the thermal process and crystallization is missing. This thesis presents numerical simulations and experimental analyses related to the formation and growth of crystals in a Zr-based bulk metallic glass. The aim is to provide a better understanding of crystallization in metallic glasses during non-isothermal processing, with special emphasis on AM by laser powder bed fusion (LPBF). The experimental investigations involved \emph{in-situ} small-angle neutron scattering measurements of nucleation and growth of crystals in a Zr-based metallic glass processed by LPBF and suction casting. It is concluded that crystals forms at a higher rate in the material processed by LPBF, as a result of the increased oxygen content. Further, the crystallization mechanisms were identified as rapid nucleation followed by diffusion-controlled growth in both materials. The numerical simulations are based on phase-field and classical nucleation and growth theory, which were developed to study the nucleation, growth, and dissolution of crystals in metallic glasses. The models have been used to predict time-temperature-transformation and continuous-heating/cooling-transformation diagrams, but also to simulate the crystallization process during LPBF by utilizing thermal finite element simulations of the laser-material interaction. The simulation results demonstrate several important aspects of crystallization in the LPBF process, such as the effect of rapid heating and cooling on the nucleation rate, the importance of the growth mode during cyclic reheating as well as the resulting gradients in particle size and density arising from localized laser processing. In particular, the results emphasize that numerical models that track the evolution of the particle size distribution are well suited for modeling crystallization in LPBF processing of metallic glass.

Key words: Amorphous metals, Crystallization, Laser powder bed fusion, Neutron scattering, Phase-field theory, Classical nucleation theory

Classification system and/or index termes (if any):

Supplementary bibliographical information:	Language English
ISSN and key title:	ISBN 978-91-8039-069-9
Recipient's notes	Number of pages 158 / Price
	Security classification

Department of Construction Sciences
Solid Mechanics

ISRN LUTFD2/TFHF-21/1065-SE(1-158)
ISBN: 978-91-8039-069-9 (print)
ISBN: 978-91-8039-070-5 (pdf)

Crystallization in additive manufacturing of metallic glass

Doctoral Thesis by

Anders Ericsson

Printed by Media-Tryck AB, Lund, Sweden
For information, address:
Division of Solid Mechanics, Lund University, Box 118, SE-221 00 Lund, Sweden
Homepage: http://www.solid.lth.se

Till Margaretha & Sven

Preface

This thesis is the result of my doctoral studies at the Division of Solid Mechanics, Lund University. First and foremost I would like to express my gratitude to my supervisors Martin Fisk and Håkan Hallberg for their support and guidance over the past five years. I am very grateful to my main supervisor Martin for his enthusiastic and persistent help. Your advice and support in the most difficult and stressful times have been crucial to me. I would also like to thank Robert Dalgliesh for the help with the SANS experiment and Adrian Rennie for teaching me about neutron scattering. My colleagues in the SSF project all deserve thanks for our inspiring discussions and productive research collaborations. Thank you to Carl-Johan Hassila, Jithin Marattukalam and Dennis Karlsson for our stimulating discussions about additive manufacturing, and Maciej Kaplan for our interesting conversations on metallic glasses. Special thanks to Martin Sahlberg and Victor Pacheco for opening my eyes to experimental research and Johan Lindwall for our collaborative work on modeling.

I must also thank all my friends and colleagues (former and present) at the Division of Solid Mechanics, for all the good times at and outside the office. It has been a joyful and knowledgeable experience and I hope we get the opportunity to work together again. Thanks to all my friends in Malmö who enrich my life with spontaneous beers, board games, football, brewing, excellent food and festivities. My good friend Emil deserves special thanks for being my partner in crime over the past two decades and for making me move to Lund in the first place. I wish to express my sincere gratitude to my family, especially my parents, for their unconditional love and support and for literally everything they have done for me. Lastly, I thank my beloved Julia for always being so understanding and loving; I am truly happy to have her in my life.

Malmö, October 2021
Anders Ericsson

Abstract

Metallic glasses are non-crystalline metals that are obtained by rapid cooling of the melt to bypass crystallization. The amorphous atomic structure shows enhanced properties relative to the crystalline counterpart. For example, enhanced mechanical properties, improved corrosion resistance, as well as excellent soft magnetic properties. The unique properties of metallic glasses make them promising for a wide range of applications, e.g. spring materials, structural components, electrical motors, and biomedical implants. One drawback is the cooling rate required for glass formation, which limits the thickness of cast components to only a few millimeters. As a solution, additive manufacturing (AM) shows promising potential to produce large-scale metallic glass components. In AM, the solidification process is short and confined to a small volume that is repetitively added. Despite the high heating and cooling rates in AM, control of crystallization is still an issue and a complete understanding of the interplay between the thermal process and crystallization is missing.

This thesis presents numerical simulations and experimental analyses related to the formation and growth of crystals in a Zr-based bulk metallic glass. The aim is to provide a better understanding of crystallization in metallic glasses during non-isothermal processing, with special emphasis on AM by laser powder bed fusion (LPBF). The experimental investigations involved *in-situ* small-angle neutron scattering measurements of nucleation and growth of crystals in a Zr-based metallic glass processed by LPBF and suction casting. It is concluded that crystals form at a higher rate in the material processed by LPBF as a result of the increased oxygen content. Further, the crystallization mechanisms were identified as rapid nucleation followed by diffusion-controlled growth in both materials.

The numerical simulations are based on phase-field and classical nucleation and growth theory, which were developed to study the nucleation, growth, and dissolution of crystals in metallic glasses. The models have been used to predict time-temperature-transformation and continuous-heating/cooling-transformation diagrams, but also to simulate the crystallization process during LPBF by utilizing thermal finite element simulations of the laser-material interaction. The simulation results demonstrate several important aspects of crystallization in the LPBF process, such as the effect of rapid heating and cooling on the nucleation rate, the importance of the growth mode during cyclic reheating as well as the resulting gradients in particle size and density arising from localized laser processing. In particular, the results emphasize that numerical models that track the evolution of the particle size distribution are well suited for modeling crystallization in LPBF processing of metallic glass.

Populärvetenskaplig sammanfattning

Nästan alla metalliska material har en ordnad atomstruktur, dvs atomerna sitter i ett visst mönster. Så är det inte för amorfa material som saknar en inbördes ordnad struktur. Glas är ett typiskt exempel på ett amorft material, men även en metallegering kan ha en amorf struktur som bildas genom snabb nedkylning. Kombinationen av metalliska egenskaper och en oordnad atomstruktur gör att glasmetaller uppvisar andra, ofta bättre, egenskaper än vanliga metaller, exempelvis högre hållfasthet, ökad rostbeständighet och minskade magnetiska förluster. Det finns därför ett stort intresse för att kunna producera glasmetalliska komponenter för en mängd applikationer. På sikt kan ett industriellt genomslag för glasmetaller leda till exempelvis implantat med förbättrad biokompabilitet, starkare lättviktsmaterial för fordons- och flygindustrin samt effektivare elmotorer.

Problem uppstår vid produktion och bearbetning av glasmetaller. När glasmetaller utsätts för förhöjd temperatur kristalliserar de och materialegenskaperna försämras. Kylhastigheten är därför kritisk vid gjutproduktion vilket medför en begränsing i komponentens storlek och oftast är tjockleken på gjutgodset enbart ett par millimeter. Här är 3D-printing en teknik med stor potential för produktion av större glasmetalliska komponenter. Med hjälp av 3D-printing kan komponenten tillverkas genom upprepad sammansmältning av ett basmaterial, t.ex. metallpulver. Stelningsprocessen begränsas då till en liten volym och korta tidspann vilket resulterar i gynnsamma förutsättningar för glasbildning. Dock är 3D-printing av glasmetall en relativt ny teknik och förståelsen för uppkomsten av kristaller under processen är inte fullständig.

Denna avhandling presenterar analyser av uppkomsten och tillväxten av kristaller i en zirkoniumbaserad glasmetallslegering. Analyserna baseras på resultat från matematiska modeller som utvecklats som en del av avhandlingen men även på experimentella mätningar. Målet har varit att öka förståelsen för den kristallisering som kan uppstå under 3D-printing av legeringen. Med hjälp av en neutronstråle har bildandet och tillväxten av kristaller studerats på nanometerskala. Analys av datan visar att kristaller bildas med en högre hastighet i ett 3D-printat material jämfört med ett gjutet material, ett resultat av den förhöjda syrehalt som kan uppstå från 3D-printingsprocessen. I den experimentella studien har även atomernas diffusionshastighet och dess inverkan på bildandet och tillväxten av kristaller studerats.

De matematiska modellerna har utvecklats i syfte att simulera bildning, tillväxt och upplösning av kristaller i glasmetaller under olika termiska och kemiska förutsättningar. Modellerna har använts för att simulera kristallisering vid olika temperaturer samt kyl-

och uppvärmningshastigheter men även under 3D-printingsprocessen. Resultaten påvisar flera viktiga aspekter av kristallisering i en 3D-printingsprocess. Exempelvis effekten av höga kyl- och uppvärmningshastigheter vid bildandet av kristaller och diffusionsinverkan på tillväxt av kristaller under cyklisk uppvärmning. Kristallisering under cyklisk uppvärmning är av särskild betydelse eftersom återuppvärmning av materialet är oundviklig under 3D-printingsprocessen.

Resultaten från forskningen presenterad i denna avhandling tillför en ökad kunskap om kristallisering i 3D-printing av glasmetaller. Sådan kunskap är nödvändig för att bättre förstå processen och på sikt kunna kontrollera den tillverkade komponentens materialegenskaper. Modellerna som utvecklats är dessutom generiska och kan appliceras på andra glaslegeringar och termiska processer, såsom svetsning, värmebehandling och gjutning.

List of appended papers

This doctoral thesis is based on the following manuscripts:

Paper A
Anders Ericsson, Martin Fisk and Håkan Hallberg
Modeling of nucleation and growth in glass-forming alloys using a combination of classical and phase-field theory
Computational Material Science 165 (2019), 167-179

Paper B
Anders Ericsson, Victor Pacheco, Martin Sahlberg,
Johan Lindwall, Håkan Hallberg and Martin Fisk
Transient nucleation in selective laser melting of Zr-based bulk metallic glass
Materials & Design 195 (2020), 108958

Paper C
Johan Lindwall, Anders Ericsson, Jithin J. Marattukalam,
Carl-Johan Hassila, Andreas Lundbäck and Martin Fisk
Simulation of phase evolution in a Zr-based glass forming alloy during multiple laser remelting
Submitted for publication

Paper D
Anders Ericsson, Victor Pacheco, Jithin J. Marattukalam,
Robert M. Dalgliesh, Adrian R. Rennie, Martin Fisk and Martin Sahlberg
Crystallization of a Zr-based metallic glass produced by laser powder bed fusion and suction casting
Non-Crystalline Solids 571 (2021) 120891

Paper E
Anders Ericsson and Martin Fisk
Modeling of diffusion-controlled crystallization kinetics in Al-Cu-Zr metallic glass
To be submitted

Own Contribution

The author of this thesis has taken the main responsibility for the preparation and writing of papers A, B, D and E. The models of crystallization in Paper A, B, C and E have been developed in collaboration with the co-authors and implemented by the main author. The thermal model in Paper B and C were developed by Johan Lindwall in collaboration with the co-authors. The flash-DSC measurements in Paper B were conducted by Sebastian Östlund and Juergen Schawe at Mettler Toledo. The small-angle scattering experiments and analysis of the data in Paper D were carried out by the main author in collaboration with the co-authors. The X-ray diffraction and electron microscopy analysis in Paper D were carried out by Victor Pacheco and Jithin J. Marattukalam, respectively.

Contents

Chapter 1

Introduction

The first metallic glass was accidentally synthesized by Duwez et al. [1] in 1960. Through rapid cooling of a droplet of an $Au_{75}Si_{25}$ (at%) alloy they had created the first non-crystalline alloy in the shape of a 10 μm thin foil. Until the 1980s, metallic glasses could only be produced under extremely high cooling rates, and samples were in the shape of thin ribbons or splat-quenched droplets [2–4]. In the mid-1980s, the discovery of metallic glasses in Pd- and La-based systems enabled the synthesis of bulk metallic glasses (BMG), which are metallic glasses with a thickness larger than 1 mm [5, 6]. Since then, BMGs have been discovered in multiple alloy systems, including in Fe-, Zr-, Ti-, Cu-, Ni-, Mg- and Co-based alloys [7–15]. To date, the largest cast component is made of the Pd-Ni-Cu-P alloy with a casting thickness of 72 mm [4, 16].

Despite the development of good metallic glass formers over the past decades, the size of components produced by traditional manufacturing techniques is still limited by the cooling rate to avoid crystallization. As an alternative, additive manufacturing is a promising technique for manufacturing BMGs without geometrical constraints. Additive manufacturing of a BMG using laser powder bed fusion was first demonstrated by Pauly et al. [17] in 2013. Since then, Fe-, Zr-, Ti- and Al-based glass-forming alloys have been successfully produced by laser powder bed fusion [17–22]. Amorphous components of sizes larger than the critical casting thickness have been produced using laser powder bed fusion in the Fe- and Zr-systems [19, 23], demonstrating the potential of the technique. Although additive manufacturing shows promising potential, the repetitive fusion of material result in a complex thermal process and the understanding of the interplay between the thermal process and crystallization is still limited [24, 25].

1.1 Research aim and objective

This thesis presents numerical simulations and experimental analyses related to the formation and growth of crystals in alloy AMZ4 ($Al_{10.4}Cu_{28.8}Nb_{1.5}Zr_{59.3}$ (at%)) [26], a Zr-based metallic glass commercially available as powder feedstock material for the LPBF process [27]. The aim is to *provide an increased understanding of the crystallization process in*

additive manufacturing of a bulk metallic glass. As part of the thesis, numerical models have been developed that can be used to predict the nucleation and growth of crystals during non-isothermal processing of a bulk metallic glass. The long-term objective is to *develop a generic model that can be applied to different glass forming systems.*

Chapter 2

Bulk metallic glasses

The following chapter presents an introduction to bulk metallic glasses (BMG), their atomic structure, properties and applications as well as the concepts of glass formation, glass forming ability and crystallization. An introduction to processing of BMGs using additive manufacturing is also included.

2.1 Atomic structure and properties

In solid metallic materials, the atoms are typically arranged in crystal lattices, that is, an ordered periodic arrangement of atoms in three dimensions. The atomic structure shows translational symmetry in each direction, which makes it possible to characterize the structure in terms of a repeated unit cell describing the smallest building block. Modifications in characteristic behavior are described in terms of divergences in the crystal lattice (e.g. crystal defects) in reference to the "perfect" periodic structure. In contrast to crystalline metals, metallic glasses exhibit an absence of long-range order of atoms and are considered to be non-crystalline. Other common words used to describe the structure are amorphous or "glassy". The word amorphous derive from ancient Greek and means "without form" or "shapeless" and serves as a simple description of the atomic ordering in metallic glass, i.e. randomly distributed atoms. The term "random" should be regarded with some care, while metallic glasses lack the long-range ordering (LRO) characteristic of crystalline metals, they do possess short-range order (SRO), in which atoms are arranged with respect to their nearest neighboring atoms, forming close-packed clustered configurations of atoms [28, 29]. The coordination number (number of nearest neighboring atoms) of the central atom can vary from cluster to cluster, constituting polyhedral atomic configurations of different sizes and chemical bonding. In addition, the SRO clusters may show inter-cluster ordering, referred as medium-range order [28, 29], in which the clusters are interconnected and efficiently packed to fill 3D-space. The SRO and MRO atomic configurations in a metallic glass are illustrated in Fig. 2.1. However, it is important to point out that there is no unique structure for a specific glass, the structure of the glass and the development of SRO and MRO atomic configurations depend on the thermal history of the material

during glass formation [30].

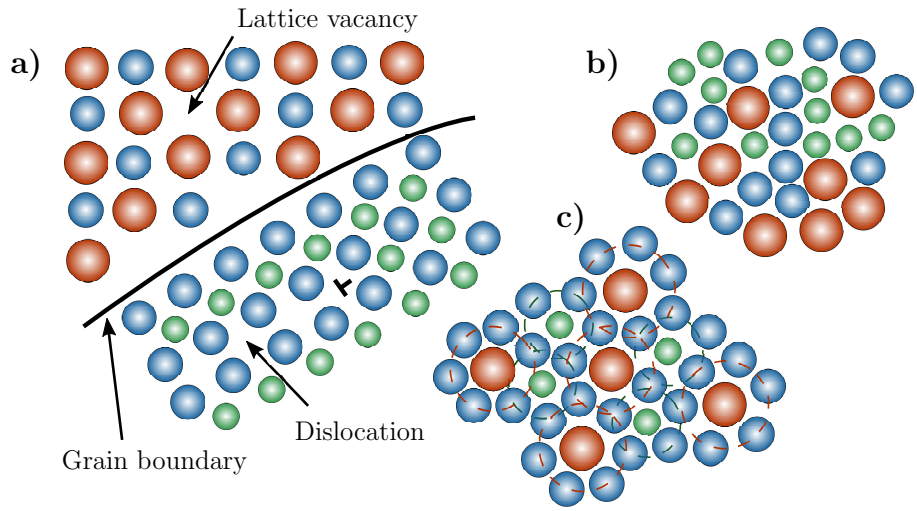

Figure 2.1: Illustration of atomic packing by a) long-range order of a polycrystalline alloy (crystal defects are indicated by the arrows) b) "randomly" distributed atoms and c) the close-packed polyhedral short-range and medium-range order of atoms in a metallic glass.

The lack of a crystalline atomic arrangement implies that the properties of metallic glasses are different in comparison to their crystalline counterparts. The absence of crystal defects such as grain boundaries, lattice vacancies, and dislocations provides high strength approaching the theoretical strength of solids, high hardness, elastic strain limit and mechanical resilience [30, 31]. The ability to store a high amount of elastic energy makes Zr-based BMGs suitable as spring materials and high sensitivity pressure sensors [30, 31]. BMGs also show high corrosion resistance, which is a desired property for biomedical applications such as biocompatible implants and surgical tools and also in applications in which the material is exposed to harsh weather conditions. In terms of tooling, the lack of grain structure allows metallic glass knives to be sharpened to an exceptionally sharp edge [31]. Fe-based metallic glasses show excellent soft magnetic properties such as low coercivity and high magnetic permeability. Because of these properties, Fe-based metallic glasses are used in magnetic transformation and induction cores, magnetic torque sensors and actuators [4].

2.2 Glass formation

When a liquid is cooled below its melting point, T_m, it is expected to solidify and form a crystalline structure (Path 1 in Fig. 2.2). The crystallization process is characterized by discontinuous changes in properties such as the volume, the specific heat capacity, and the

viscosity (see Fig. 2.2). However, crystallization can be postponed to temperatures below T_m, which is known as undercooling. The undercooling is possible due to the existence of an energy barrier for nucleation of the crystalline phase, arising from the energy cost of the interface between the crystalline nuclei and the liquid. With increasing undercooling, the density of the liquid gradually increases, decreasing the free volume available for atomic motion. The decrease in free volume is reflected by an increase in viscosity. Upon further cooling the viscosity eventually becomes so high that the relaxation time for viscous flow is too long for the liquid to internally equilibrate within the given time[32, 33] (Path 2 in Fig. 2.2). The structure of the liquid becomes "frozen-in" and behaves for all practical purposes as a solid. This state of matter is referred to as glass, and the temperature at which the structural arrest occurs is referred to as the glass transition temperature T_g.

Upon annealing, the glass shows structural relaxation (Path 3 in Fig. 2.2), also known as aging, in which the atomic free volume decreases with time and the glass eventually attains the denser state of the equilibrium liquid. Hence the glass transition is a reversible process in which the glass can transform back to the undercooled liquid state upon annealing or heating. The amount of free volume that is annealed depends on the deviation from internal equilibrium during glass formation, a glass obtained at a higher cooling rate is structurally less relaxed than a glass obtained at a lower cooling rate [34]. Further annealing or heating of the undercooled liquid state eventually results in crystallization.

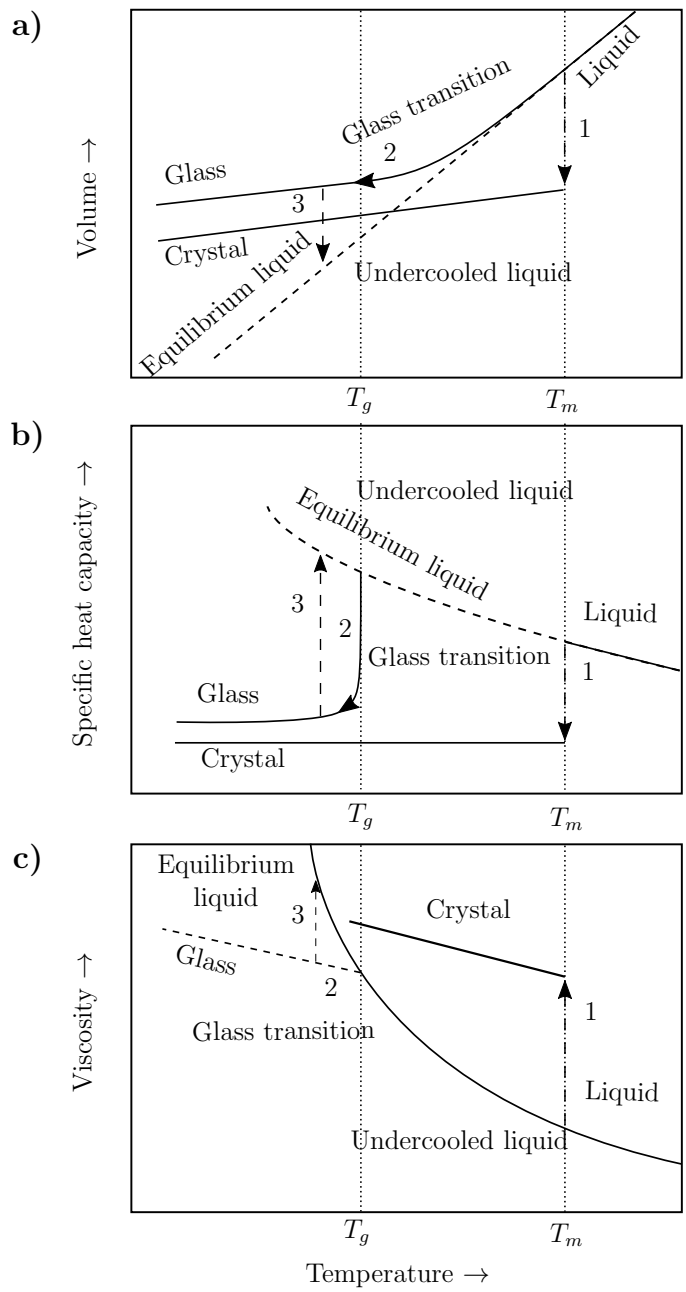

Figure 2.2: Illustration of changes in properties during 1. crystallization, 2. glass formation and 3. structural relaxation of a glass. From top to bottom: a) volume, b) specific heat capacity and c) viscosity.

2.3 Crystallization

A fundamental requirement for glass formation is that crystallization is suppressed. In general, crystallization is detrimental to the properties of metallic glasses, as it forms at the expense of the amorphous material. Suppression of crystallization is achieved by cooling the liquid alloy sufficiently fast. The minimum cooling rate required to achieve glass formation is denoted as the critical cooling rate R_c and serves as a metric of the alloy's glass forming ability (GFA). The glass forming ability of an alloy is therefore equivalent to the resistance to crystallization. The critical cooling rate is best depicted in terms of a time-temperature-transformation (TTT) diagram as shown in Fig. 2.3. The diagram shows the time it takes for an alloy to crystallize at different temperatures under isothermal conditions, which typically forms a C-shaped curve because of the temperature dependent thermodynamic and kinetic material properties. At temperatures close to the melting point, the liquid state is close to thermodynamic equilibrium and the driving force for crystallization is low. While at low temperatures, the thermal activation required for atomic mobility (diffusion) is low. Thus the rate of crystallization is highest at some intermediate temperature between the melting point and the glass transition. The critical cooling rate R_c is the rate required to bypass the "nose" of the TTT-diagram of the competing crystalline phases and is often, as discussed in [30], expressed using the linear expression

$$R_c = \frac{T_m - T_c}{t_c} \tag{2.1}$$

where T_c and t_c is the temperature and the time at the nose of the TTT-diagram, respectively. Since the cooling rate is dependent on the component size during a casting process, the critical casting thickness is also a metric of GFA. Unfortunately, the critical cooling rate is difficult to determine in practice and can only be accurately measured under controlled cooling conditions. Further, the critical casting thickness depends on the casting method and mold geometry. Therefore, other metrics have been developed based on thermodynamic and kinetic transition temperatures. Turnbull derived the well-known reduced glass transition temperature $T_{rg} = T_g/T_l$ [35], where T_l is the liquidus temperature. Another metric was presented by Inoue et al. [36], which was defined as the width of the undercooled liquid region $\Delta T_x = T_x - T_g$, where T_x is the temperature of crystallization upon heating. The quantities T_g and T_x are illustrated in Fig. 2.3 during a typical heating sequence from the glassy state. In theory, a high value of T_{rg} or ΔT_x is an indicator of high GFA of an alloy. The metrics had various successes in predicting the GFA in different alloy systems [30].

Prediction of GFA is of great importance in the development of new glass forming alloys. Inoue formulated three well known empirical criteria for bulk metallic glass formation [37]. According to Inoue [37], bulk metallic glass formation is more likely in an alloy system with, 1) more than three alloying elements 2) greater than 12% atomic size mismatch and 3) negative heats of mixing among the elements. Compliance with the above rules increases the degree of dense atomic packing and the formation of atomic configurations on a short-range scale. In terms of crystallization, the topological and chemical short-range atomic

configurations stabilize the liquid thermodynamically and make it more difficult for the atomic rearrangement necessary for long-range diffusion.

The characteristic temperatures T_g, T_x, and T_m can be measured during the heating of an as-prepared glass using a differential scanning calorimeter (DSC). DSC is a thermoanalytical technique, which measures the required heat flow to keep or increase the temperature of a material. Since heat is released or absorbed during phase transformations, the DSC can be used to detect the temperature at which glass transition, crystallization, and melting occur in a single measurement [38]. Therefore it has been widely used to measure the thermal stability and characteristic temperatures of glass forming alloys [30]. The DSC technique was utilized in Paper B to measure the time for crystallization at different temperatures and construct a TTT-diagram of the Zr-based alloy AMZ4.

DSC techniques measure the heat flow of the transformation and do not provide information on the crystallographic structure, shape or distribution of crystals. X-ray diffraction (XRD) can be used to characterize the atomic structure of an alloy. For an amorphous structure, the X-rays scatter isotropically and the diffraction pattern appears as a broad diffuse halo because of the absence of long-range atomic ordering [30]. In contrast, for crystallized samples, the X-ray beam is scattered in preferred directions caused by the periodic ordering of the crystal lattices and distinct diffraction peaks appear in the diffraction pattern. XRD can provide information on the inter-atomic distances and crystallographic structure [21, 39]. Small angle scattering (SAS) is another experimental technique that can be used to probe crystallization on a length scale that ranges between 1 nm and a few 100 nm [40–43]. SAS can be used to estimate the size and distribution of crystalline particles in a bulk volume. Both XRD and SAS were used in Paper D to measure crystallization in a Zr-based BMG. The SAS technique is described in more detail in Chapter 3.

2.3.1 Crystallization modes in metallic glass

Crystallization in metallic glasses occurs by nucleation and growth. Depending on the composition, the crystallization of the metastable amorphous phase proceed by one of the following transformation modes [30, 44]:

- **Polymorphous crystallization:** The crystalline phase forms without any significant change in composition. Since there is no need for long-range diffusion, the growth is governed by the rate of atomic attachment at the interface. Such transformation can only occur when the composition of the amorphous material and the crystals are equal or close to equal.

- **Primary crystallization:** Crystallization occurs through the formation of a phase with a different composition than the amorphous material. As the formation proceeds, the amorphous phase will become enriched/depleted of elements until the crystallization reaches a metastable equilibrium. The change in the composition of the amorphous phase changes the driving force of crystallization of other phases that

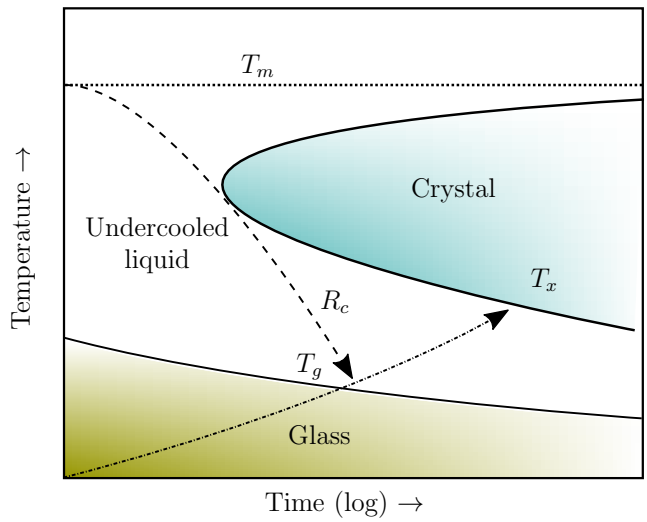

Figure 2.3: Illustration of a time-temperature-transformation (TTT) diagram, cooling curve for glass formation (dashed) and heating curve for crystallization (dash-dotted).

become increasingly likely to form. During primary crystallization, the rate of the transformation is dictated by long-range diffusion.

- **Eutectic crystallization:** Phases form simultaneously in a eutectic reaction. This reaction shows no composition difference between the eutectic phases and the residual amorphous matrix. Therefore it is similar to polymorphous crystallization, with the exception that two or more phases constitute the crystal.

The three crystallization modes are illustrated in Fig. 2.4. Among the three modes, the primary crystallization mode is the most common [30, 44]. One reason for this is that glass forming alloys are developed with the purpose to resist crystallization. Alloy compositions that crystallize in a primary mode require long-range diffusion, which is hindered by the preferred topological and chemical atomic arrangement in the liquid. A metallic glass can, however, crystallize through combinations of the modes outlined above as multiple crystalline phases usually form. For example, primary crystallization of one phase can change the composition of the matrix which results in polymorphous crystallization of another phase. Other complex crystallization paths have also been observed and the amorphous phase has in some cases been reported to separate through spinodal decomposition [45], resulting in two amorphous phases of different compositions that can crystallize through different modes.

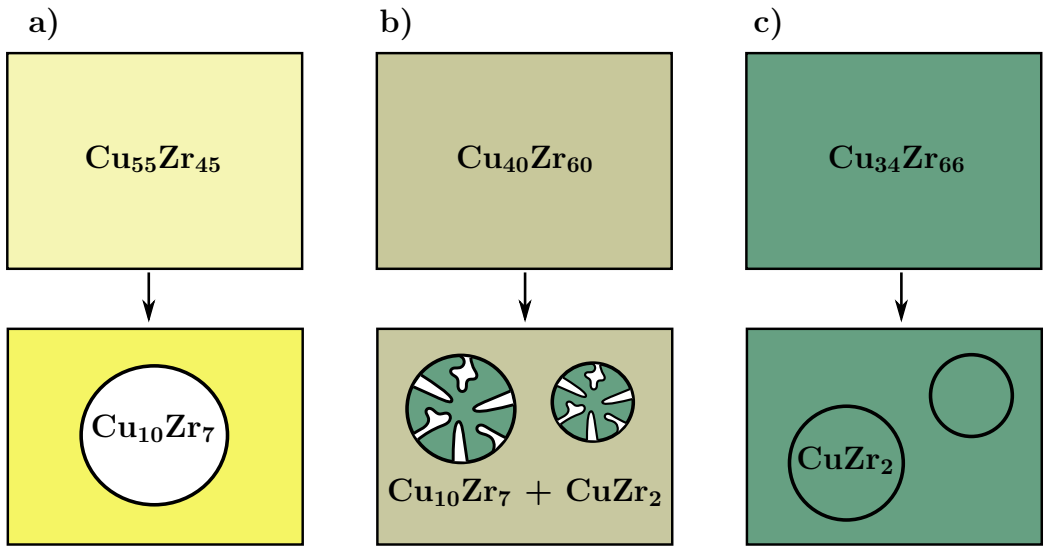

Figure 2.4: Illustration of crystallization modes in a Cu-Zr metallic glass of different composition. a) primary crystallization of $Cu_{10}Zr_7$, b) eutectic crystallization of $Cu_{10}Zr_7$ + $CuZr_2$ and c) polymorphic transformation of $CuZr_2$.

2.4 Additive manufacturing

The fabrication of metallic glasses requires high cooling rates, which limit the size and shape of components produced by traditional manufacturing techniques. The cooling rate in a casting process is dependent on the temperature gradient across the bulk material and thus the thickness of the mold [3]. From this perspective, metallic additive manufacturing techniques offer unique possibilities for the fabrication of metallic glass components without geometrical restrictions. Other advantages of AM are the design of complex geometries, efficient material usage as well as lean manufacturing [46]. Laser powder bed fusion (LPBF), also known as selective laser melting (SLM), is the most widely used additive manufacturing technique for the fabrication of BMGs [25]. In LPBF, the metallic component is manufactured by localized melting and fusion of a powder bed, building the component from the bottom and up, layer by layer. The localized laser processing provides a rapid dissipation of heat and hence high cooling and heating rates, which can be utilized to manufacture metallic glass components of characteristic size larger than the critical casting thickness [19, 24, 47]. So far, Fe-, Zr-, Ti- and Al-based glass-forming alloys have been successfully produced by LPBF [18–20, 22].

In the perspective of crystallization of metallic glasses, additive manufacturing is different from traditional production techniques. In traditional production by solidification such as casting or melt spinning, the glass is obtained by cooling from the melt to room temperature and the whole component is vitrified through a single cooling sequence. In additive manufacturing, confined volumes are repetitively added through local solidifica-

tion. This implies that the already vitrified material will be reheated. The cooling rates can be as high as $10^3 - 10^8$ Ks^{-1} [24], which is higher than the typical critical cooling rate of BMGs ($< 10^3 \mathrm{Ks}^{-1}$) [30]. Thus most crystallization does not arise from the cooling process, but rather from the cyclic reheating as new material is added. The temperature history experienced by a material point in the vicinity of the melt pool from the LPBF simulation in Paper B is shown in Fig. 2.5.

Although LPBF is a promising technique for BMG production, there are several challenges inherent to the technique. Defects such as pores, lack of fusion and cracks may arise from the process [25]. The extent to which these defects form depends on the process parameters such as laser power (P), scanning speed (v), hatching distance (h) and layer thickness (t). The parameters can be combined to form a measure of the volume energy density (VED) during the process, given by

$$\mathrm{VED} = \frac{P}{vht} \tag{2.2}$$

In general, a too low value of VED causes a lack of fusion of the powder and increases the porosity of the component [24]. Pores are stress concentrations and can act as crack nucleation sites. Cracks can also arise due to residual stresses caused by the high thermal gradients during the process. On the contrary, a too high value of VED may induce crystallization since more material is exposed to higher temperatures. Therefore, the process parameters have to be tuned to find the optimal value of VED, which results in a high relative density and a low amount of crystals in the final component [24]. Besides the process parameters, the scanning strategy (illustrated in Fig. 2.6) is also important as it affects the accumulation of heat during the build process as well as it determines where and when the material is reheated [25]. For example, in the case of Zr-based BMGs, a scanning strategy involving remelting of each layer using a lower value of VED has been found to result in less porosity and crystallization than single scans with a higher VED [48]. Identifying the optimal processing conditions of metallic glasses requires careful optimization of many tunable parameters and scanning strategies.

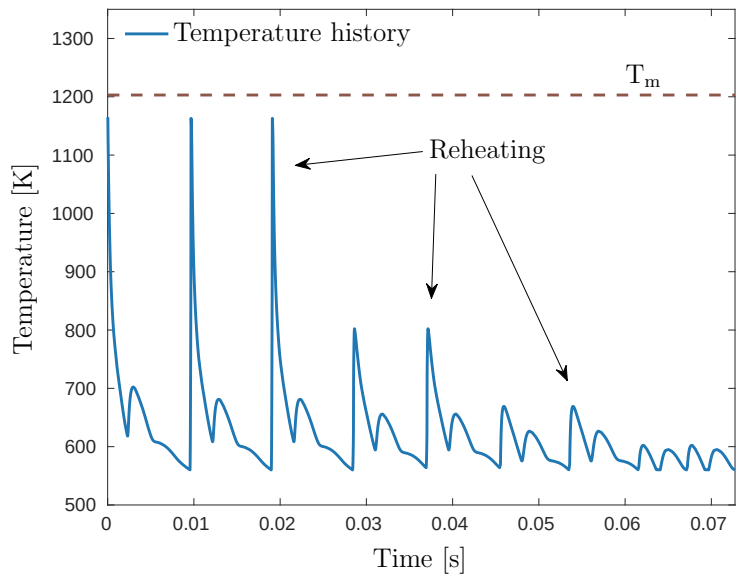

Figure 2.5: Temperature history obtained from the thermal LPBF simulation in Paper B, representative of the x-y remelting scanning strategy in Fig. 2.6. The melting temperature T_m is indicated by the horizontal dashed line. As new layers are added or existing layers are remelted, the already solidified material experience reheating and is exposed to crystallization.

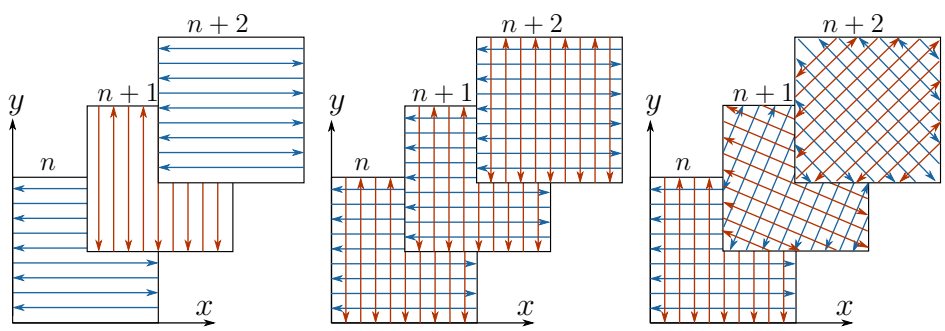

Figure 2.6: Illustration of different scanning strategies for layers n, $n+1$ and $n+2$. a) Alternating single scans in x- and y-direction, b) x-y remelting of each layer and c) x-y remelting of each layer with rotation.

Chapter 3

Small angle neutron scattering measurements

Small angle scattering (SAS) is a technique used to investigate structures that are generally in the characteristic size range of 1 nm to some 100 nm. Information of the size regime is obtained by measuring the intensity of the scattered beam at low angles, hence the name small angle scattering. The observed scattering profiles depend on the phase difference between coherent neutron or X-ray waves scattered at different locations in the sample. The SAS technique is useful for detection of nanosized particles that forms during the crystallization of BMGs [40–43]. Since the incident beam illuminates the bulk material over a relative large volume, information on the size distribution of these particles can be obtained.

The two primary sources for SAS experiments are X-ray (small angle X-ray scattering, SAXS) and neutron sources (small angle neutron scattering, SANS), both sources have their respective advantages and can provide information complementary to one and the other [49]. For example, X-rays are scattered by electrons, and neutrons are scattered by the center of the atomic nucleus. Therefore neutrons and X-rays provide different contrast of the structure in the material. Neutrons also provide better penetration depth but at a lower flux than X-rays. SANS was used in Paper D to characterize the crystallization in a Zr-based metallic glass produced by laser powder bed fusion and suction casting. A neutron source was chosen to probe the role of oxygen on crystallization. The characterization method is outlined in the subsequent sections along with some main results.

3.1 Fundamental principles of small angle neutron scattering

In SANS experiments, the aim is to determine the probability that a neutron, with incident wave vector $\boldsymbol{k_0}$, is scattered into a state with wave vector $\boldsymbol{k}$. The intensity of the scattered

beam is therefore measured as a function of the scattering vector $\boldsymbol{q}$ defined as

$$\boldsymbol{q} = \boldsymbol{k} - \boldsymbol{k_0} \tag{3.1}$$

For elastic scattering, the wave number (and thus wavelength and frequency) of the incident and scattered beam is equal ($|\boldsymbol{k}| = |\boldsymbol{k_0}|$) and magnitude of the scattering vector $|\boldsymbol{q}| = q$, known as momentum transfer, is given by

$$|\boldsymbol{q}| = q = \frac{4\pi}{\lambda} \sin\theta \tag{3.2}$$

where 2θ is the scattering angle and λ is the wavelength of the beam. Eq. (3.2) defines the scattering geometry and its dependence on the energy of the beam (the wavelength). The flux Φ_S of the scattered neutrons varies with the scattering angle (or scattering vector) and is normalized by the flux Φ_0 of the incident neutrons. The ratio Φ_S/Φ_0 is defined as

$$\frac{d\sigma}{d\Omega} = \frac{\Phi_S}{\Phi_0} \left[\frac{\text{cm}^2}{\text{sterad}}\right] \tag{3.3}$$

where σ is called the scattered cross section, having the unit of cm^2 and depends on the scattering lengths b of the elements in the investigated material [49]. The scattering length is the "strength" or amplitude of the scattering. For neutron scattering, the scattering lengths vary irregularly across the periodic table and is determined by quantum mechanics of the neutron-nucleus interaction. The variable Ω denotes the scattered solid angle, i.e. the amount of field of view from the scattered point, and is given in the dimension of a *steradian*.

The derivative $d\sigma/d\Omega$ in Eq. (3.3) is called the *differential scattering cross section* and represents the probability that a neutron is scattered into a unit solid angle in a given direction. The units of the differential scattering cross section arises from the properties of the scattering of a incident planar wave Φ_0 $[\text{s}^{-1}\text{cm}^{-2}]$ into a spherical wave of units Φ_S $[\text{s}^{-1}\text{sterad}^{-1}]$. A schematic of the SANS experiment is illustrated in Fig. 3.1.

The intensity of the scattered beam will be of different magnitude depending on the sample thickness, hence the differential scattering cross section is normalized using the illuminated sample volume V, providing

$$\frac{d\Sigma}{d\Omega}(\boldsymbol{q}) = \frac{1}{V}\frac{d\sigma}{d\Omega}(\boldsymbol{q}) \tag{3.4}$$

which has the dimension of $[\text{cm}^{-1}\text{sterad}^{-1}]$. The unit of the solid angle is often omitted and the scattering curves are presented in so-called absolute units of $[\text{cm}^{-1}]$. As will be shown in Section 3.2, the scattering curves in absolute units are essential for calculating the number density or volume fraction of the crystalline particles. In practice, the scattering curves in absolute units are typically obtained by correcting the measured scattering intensity for detector efficiencies, sample transmission and background scattering and by calibrating the data to measurements of a reference sample. For isotropic scattering patterns, the 2D data is reduced to 1D plots ($\frac{d\Sigma}{d\Omega}(q)$ *vs* q) through azimuthal averaging of the data around the beam center (angular direction of Ψ in Fig. 3.1). In Paper D, the data correction and reduction was performed using the Mantid software [50].

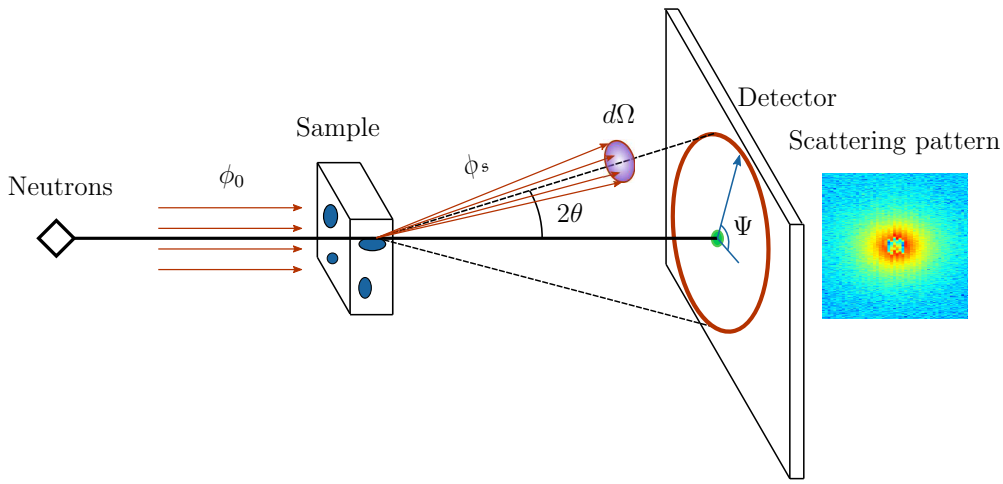

Figure 3.1: Schematic illustration of a small angle neutron scattering experiment.

3.2 Quantitative analysis of data

The amplitude of the scattered spherical wave relative to the incident planar wave can be described by a series of wave functions on the form [49]

$$A(\boldsymbol{q}) = \sum_j B_j \exp\left(-i\boldsymbol{q}\cdot\boldsymbol{r}_j\right) \tag{3.5}$$

where B_j is the generalized scattering length of neutron j with position $\boldsymbol{r}_j$. Describing the distribution of neutrons as a continuous function and Eq. (3.5) can be rewritten as

$$A(\boldsymbol{q}) = \int_V \rho^*(\boldsymbol{r}) \exp(-i\boldsymbol{q}\cdot\boldsymbol{r}) d\boldsymbol{r} \tag{3.6}$$

where the sum over all scattered neutrons in Eq. (3.5) has been replaced with an integral over the illuminated sample volume V and the discrete generalized scattering lengths B_j has been replaced by a continuous function for the scattering length density $\rho^*(\boldsymbol{r})$. The differential scattering cross section describes the probability of neutron scattering and is related to $A(\boldsymbol{q})$ through $d\sigma/d\Omega(\boldsymbol{q}) = |A(\boldsymbol{q})|^2$ [49], therefore

$$\frac{d\Sigma}{d\Omega}(\boldsymbol{q}) = \frac{1}{V}\left|A(\boldsymbol{q})\right|^2 = \frac{1}{V}\left|\int_V \rho^*(\boldsymbol{r}) \exp\left(-i\boldsymbol{q}\cdot\boldsymbol{r}\right) d\boldsymbol{r}\right|^2 \tag{3.7}$$

which shows the relationship between the measured differential scattering cross section and the distribution of scattering length density in the sample. Eq. (3.6) is essentially the Fourier transform of the scattering length density $\rho^*(\boldsymbol{r})$ from real space of $\boldsymbol{r}$ to Fourier

space of $\boldsymbol{q}$, also known as reciprocal space. The Fourier transform is a central concept in the analysis of small angle scattering data and allows to derive a model for $\frac{d\Sigma}{d\Omega}(\boldsymbol{q})$ based on knowledge of $\rho^*(\boldsymbol{r})$. The model allows for a quantitative interpretation of the measured differential scattering cross section.

In the case of isotropic scattering of spherical particles, the differential scattering cross section is simply a function of momentum transfer q and Eq. (3.7) can be integrated using spherical coordinates [51], resulting in

$$\frac{d\Sigma}{d\Omega}(q) = \frac{n}{V}\left[\int_0^\infty \rho^*(r)\,\frac{\sin(qr)}{qr} 4\pi r^2 dr\right]^2 \tag{3.8}$$

where n is the number of particles and the integral defines the scattering of a spherically symmetric particle as a function of the radial direction r across the particle. Assuming a uniform scattering length density across the particle and the matrix, Eq. (3.8) can be evaluated as

$$\frac{d\Sigma}{d\Omega}(q) = N\left(\Delta\rho^*\right)^2 \left[V_p F(q,R)\right]^2 \tag{3.9}$$

where $N = n/V$ is the number density of particles, $\Delta\rho^* = \rho_p - \rho_m$ is the difference in scattering length density between the particle and the matrix, $V_p = 4\pi R^3/3$ is the particle volume and $F(q,R)$ is called the form factor, which for a spherical particle with radius R is expressed as

$$F(q) = \frac{3\left[\sin(qR) - qR\cos(qR)\right]}{(qR)^3} \tag{3.10}$$

The model of the differential scattering cross section presented in Eq. (3.9) is a suitable representation of scattering arising from spherical particles of the same size. However, this is rarely the case for nucleation and growth of crystals and more often the particle size varies across the sample. To consider polydispersity in the model of the scattering data, the size dependent factors in Eq. (3.9) are weighted by a normalized size distribution $f(R)$ [52], which provides

$$\frac{d\Sigma}{d\Omega}(q) = N\left(\Delta\rho^*\right)^2 \int_0^\infty f(R)\left[V_p F(q,R)\right]^2 dR \tag{3.11}$$

The size distribution is chosen based on knowledge of how the particles form and grow in the material. For a random nucleation and growth process, a log-normal size distribution has been recognized as a suitable choice, as noted in [53], and $f(R)$ is then written as

$$f(R) = \frac{1}{\sigma R\sqrt{2\pi}} \exp\left(-\frac{1}{2\sigma^2}\ln\left(\frac{R}{R_{med}}\right)^2\right) \tag{3.12}$$

where R_{med} is the median size of the particles and σ is a parameter representing the width of the distribution.

The model presented in Eq. (3.11) is used to fit the scattering data presented in Paper D. Three fitting parameters, R_{med}, σ and N are included, which fully describes the particle

size distribution. These parameters are fitted to the experimental data in a time series using the non-linear least squares method. For each data set, the fit from the previous solution is used as initial guess. Besides the parameters of the particle model, a Porod model of the background scattering was included for which $\frac{d\Sigma}{d\Omega}(q) \propto q^4$ [49]. The background model was fitted to the scattering intensity of the samples at room temperature to account for the scattering of pores.

The differential scattering cross-section of AMZ4 samples annealed at 370 °C and the fitted model is presented in Fig. 3.2 a) at different times. The corresponding crystal size distributions are shown in Fig. 3.2 b). An important property of the particle model is that the differential scattering cross section depends linearly on the number of particles in the sample (number density N), whereas it scales nonlinearly as a function of the particle size R. This is seen if $V_p = 4\pi R^3/3$ is inserted into Eq. (3.9) to obtain $d\Sigma/d\Omega(q) \propto R^6$, hence the magnitude of the scattering signal is predominantly defined by the particle sizes rather than the concentration of particles. As seen in Fig. 3.2, the scattering peaks of the LPBF processed and cast samples appear at different momentum transfer, which shows that the crystallization occur at different characteristic length-scales in the cast material and the material processed by LPBF. The LPBF processed sample crystallize with a higher number density and smaller average particle size than the cast sample. In Paper D, this difference was attributed to the elevated oxygen content of the LPBF processed material, which lowers the thermodynamic stability against crystallization.

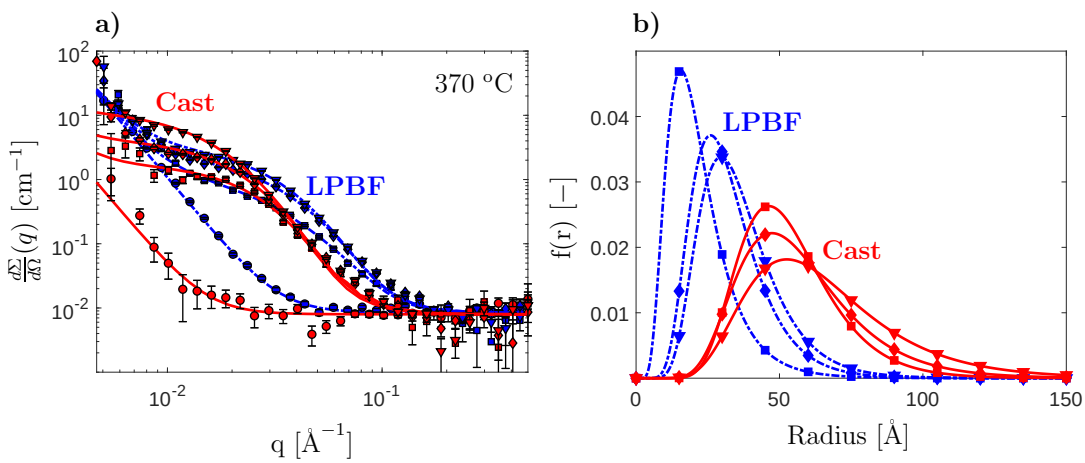

Figure 3.2: (a) Differential scattering cross-section $\frac{d\Sigma}{d\Omega}(q)$ and fitted model for cast (solid red line) and LPBF (dash-dotted blue line) processed AMZ4 during annealing at 370 °C. The symbols with uncertainty bars represent the experimental data at different times and the lines are the model curves. The following data are presented: room temperature measurement (●), 0 min (■), 30 min (♦) and 90 min (▼). (b) Log-normal size distributions at the corresponding times for cast (solid red line) and LPBF (dash-dotted blue line) samples.

Chapter 4

Microstructural modeling

In the following chapter, the models used to predict crystallization are described. The phase-field theory employed in Paper A is presented in Section 4.1 together with some results from the simulations. The classical nucleation and growth theory used in Papers C, B and E is described in Section 4.2 for different growth models, followed by a presentation of the thermodynamic models and the interfacial energy in Sections 4.3 and 4.4. Similarities and differences between the phase-field and classical models as well as the different thermodynamic models are discussed. In Section 4.5, results from the application of the classical nucleation and growth theory to the LPBF process of alloy AMZ4 in Papers B and C are presented.

4.1 Phase-field theory

The phase-field method is widely recognized as a competent computational method to model the microstructure evolution of metallic alloys. The method has been adopted for a wide range of phase transformation problems such as solidification processes and dendritic growth [54–56], solid state recrystallization and precipitation [57, 58] as well as nucleation processes [59]. This section outlines the phase-field model used in Paper A to model the nucleation and growth of intermetallic phases from an undercooled Cu-Zr alloy.

In the phase-field method, the microstructure is described by a set of non-conserved field variables, here denoted by $\phi_i(\mathbf{r}, t)$, $i = 1 \dots n_\phi$. The phase-field variables are continuous in space $\mathbf{r}$ and time t and represent the atomic ordering at different positions in the material. In a similar manner, mass distribution can be represented by conserved field variables $c_i(\mathbf{r}, t)$, $i = 1 \dots n_c$, which describes the local mixture of alloying elements. The composition variables are, like the phase-field variables ϕ_i, continuous in space and time and vary smoothly across interfaces.

In the work presented in Paper A, a single phase-field variable ϕ is used to describe the difference in atomic ordering of an undercooled liquid phase to a crystalline phase. A global conserved field variable c is used to represent the mass distribution of Zr in the Cu-Zr alloy. The field variables ϕ and c are coupled by the total energy of the system

[54, 60, 61], given by

$$F(\phi, c, T) = \int_V f(\phi, c, T) + \frac{\epsilon^2}{2}(\nabla\phi)^2 dV \tag{4.1}$$

where T is the temperature and V is the volume of the system. $f(\phi, c, T)$ is the free energy density arising from the physics described by the model. The second term in Eq. (4.1) provides an energy cost to the creation of interfaces where $|\nabla\phi| > 0$, therefore the gradient energy coefficient ϵ is related to the energy and thickness of the interfacial region between the crystalline and liquid phase. Different models have been proposed for the free energy density [60]. In Paper A, the free energy density was constructed using the model proposed by Kim et al. [61], which make use of the bulk free energy density in the solid $f_S(c_S, T)$ and in the liquid $f_L(c_L, T)$ and the interpolation polynomials $h(\phi)$ and $g(\phi)$, providing

$$f(c, \phi, T) = h(\phi) f_S(c_S, T) + [1 - h(\phi)] f_L(c_L, T) + w g(\phi) \tag{4.2}$$

where c_S and c_L are the composition fields of the solid and liquid phase, respectively. These are related to the global composition field through $c = h(\phi)c_S + [1 - h(\phi)]c_L$ and through the additional constraint of local equilibrium given by

$$\mu = \frac{\partial f}{\partial c} = \frac{\partial f_S(c_S)}{\partial c_S} = \frac{\partial f_L(c_L)}{\partial c_L} \tag{4.3}$$

The parameter w is related to the width and energy of the interfacial region and thus also to the gradient energy coefficient ϵ. The main advantage of the formulation of $f(c, \phi, T)$ in Eq. (4.2) is that $f_S(c_S, T)$ and $f_L(c_L, T)$ can be straightforwardly obtained from temperature and composition dependent thermodynamic databases. In Paper A, $f_S(c_S, T)$ and $f_L(c_L, T)$ was fitted to a CALPHAD database of the Cu-Zr system using composition dependent polynomial functions.

The evolution of the phase-field variable ϕ, and the composition field variable c are given by the Allen-Cahn and Cahn-Hilliard equations [62], which relate the time derivatives to the variational derivatives of the total energy. The evolution equations appear as

$$\frac{\partial \phi}{\partial t} = -M_\phi \frac{\delta F}{\delta \phi} \tag{4.4a}$$

$$\frac{\partial c}{\partial t} = \nabla\big[M_c \nabla \frac{\delta F}{\delta c}\big] \tag{4.4b}$$

where M_ϕ and M_c are mobility coefficients describing the rate of atomic attachment at the interface and the atomic mobility of Zr, respectively. These coefficients may adopt different values depending on the physics of the propagating interface. A relationship between M_ϕ and M_c for diffusion-controlled growth was derived in [63], which was utilized in Paper A.

The phase-field model described above was used to study the nucleation and growth of intermetallic phases in the Cu-Zr system. The work of formation to nucleation and the properties of the critical nucleus was obtained by solving the unstable equilibrium

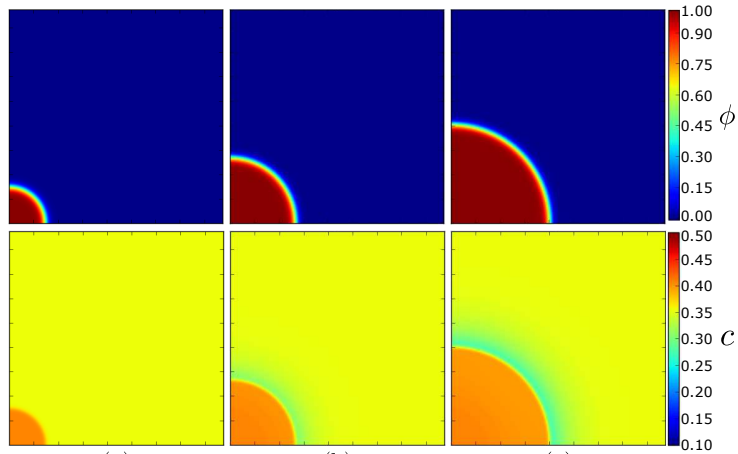

Figure 4.1: Growth of a $Cu_{10}Zr_7$ supercritical nucleus from a supercooled liquid of initial composition $Cu_{64}Zr_{36}$ at $T = 800$ K. Top row: The evolution of the phase-field variable ϕ, i.e. the migration of the interface, at times (a) $t = 0$ s, (b) $t = 1.04 \cdot 10^{-6}$ s and (c) $t = 1.30 \cdot 10^{-6}$ s. Bottom row: The evolution of the global composition field variable c at the same instances in time, showing the depletion of Zr in front of the interface as the nucleus grows.

of Eqs (4.4a) and (4.4b). Further, the spatial solution of ϕ and c was used to initiate growth simulations of the supercritical nucleus under different conditions. Fig. 4.2 shows the evolution of the field variables ϕ and c of the intermetallic $Cu_{10}Zr_7$ phase from a supercooled liquid of initial composition $Cu_{64}Zr_{36}$. As the nucleus grows, the region in front of the interface becomes depleted of Zr because of the compositional difference between the nucleus and the liquid. A composition gradient develops which dictates the rate of the transformation and as a consequence, the growth rate becomes lower with increasing size as the depletion zone extends further into the matrix. The growth rate as a function of nucleus size is shown in Fig. 4.2. For comparison the growth rate of a $Cu_{10}Zr_7$ nucleus under polymorphic conditions is also included. The polymorphic conditions result in a higher growth rate that reaches a constant value at large particle sizes, in contrast to the diffusion-controlled growth, which decreases with particle size, following a $\propto \sqrt{t}$ dependence.

Atomic ordering is described as a continuum in phase-field theory. For nucleation problems, this provides a more realistic representation of a nano-sized nucleus for which the difference in atomic ordering between the crystal and liquid may be ambiguous. Classical nucleation theory is a sharp interface theory, meaning that the nucleus is assumed to have bulk crystalline properties, also known as the capillarity approximation. As a consequence, phase-field theory results in a lower work of formation of the nucleus in comparison to classical nucleation theory. This discrepancy was observed in Paper A for the $Cu_{10}Zr_7$ phase. At large undercooling, the properties of the crystal nucleus in the phase-field

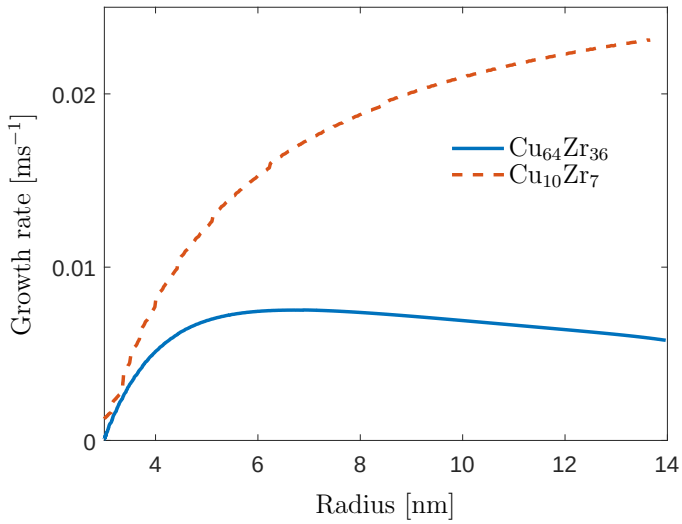

Figure 4.2: Computed growth rate of the $Cu_{10}Zr_7$ phase as a function of nucleus size: primary crystallization from a $Cu_{64}Zr_{36}$ liquid (solid blue), polymorphic crystallization (dashed red). The figure shows the difference in growth rate between the two transformation modes.

model deviate from the capillarity approximation of classical nucleation theory and as a result, a lower energy barrier to nucleation is obtained. This is especially true far from equilibrium where the driving force for crystallization is high. The phenomenon requires a size correction of the interfacial energy when modeling nucleation in glass forming liquids using classical nucleation theory, as further discussed in Section 4.4.

4.2 Classical nucleation and growth theory

In contrast to phase-field theory, classical nucleation and growth theory is a sharp interface theory in which the interface is described as a discontinuity in material properties, such as atomic ordering and chemical composition. Consequently, boundary conditions arise at the interface, which makes the description of complex particle morphologies difficult. For spherical particles, the equations describing nucleation and growth become simplified, which can be used to simulate the evolution of particle size distributions. The following sections describe classical nucleation theory (CNT) and sharp interface models for polymorphic and diffusion-controlled growth of spherical particles.

4.2.1 Nucleation

Nucleation is the initial step of the crystallization process, during which atoms agglomerate to create stable crystalline clusters that can grow autonomously. The nucleation is a stochastic process and the rate of nuclei formation is inherently related to a probability of nucleus formation. Following statistical mechanics [64], the probability of n atoms to exist in a crystalline state $P(n)$ depends on the work (energy) of nucleus formation $W(n)$ and can be described as

$$P(n) \propto \exp\left(\frac{-W(n)}{k_B T}\right) \tag{4.5}$$

where T is the absolute temperature and k_B is the Boltzmann constant. Within the classical theory of nucleation, the interface between the nucleus and the matrix is assumed sharp and the work of nucleus formation for a spherical nucleus is expressed as [64]

$$W(n) = -nd_c' + (36\pi)^{1/3}\bar{v}^{2/3}n^{2/3}\sigma \tag{4.6}$$

where d_c' is the chemical driving force per atom, $\bar{v}$ is the mean atomic volume and σ is the interfacial energy per unit area. The chemical driving force d_c' is further described in Section 4.3. In Eq. (4.6), the terms involving d_c' and σ describe the thermodynamic competition between the bulk energy release of the transformation and the cost of the creation of the interface. Thus, there exists a maximum work of formation $W(n^*)$ at a critical size denoted as n^*. The maximum work of formation, or critical work of formation, $W(n^*)$, is found by solving $dW(n)/dn = 0$, providing

$$W(n^*) = \frac{16\pi\bar{v}^2\sigma^3}{3(d_c')^2} \tag{4.7}$$

which corresponds to the critical cluster size, n^*, through

$$n^* = \frac{32\pi\bar{v}^2\sigma^3}{3\left(d_c'\right)^3} \tag{4.8}$$

Clusters of size n^* are in unstable equilibrium; those smaller than n^* (often called embryos) tend to dissolve while clusters larger than the critical size will on average grow. The equations in Eq. (4.6) and (4.8) can be written in terms of the radius. The work of formation for a spherical cluster is then

$$W(r) = -\frac{4\pi}{3V_m}r^3 d_c + 4\pi r^2\sigma \tag{4.9}$$

and the critical radius becomes

$$r^* = \frac{2\sigma V_m}{d_c} \tag{4.10}$$

where the relationship $n\bar{v} = 4\pi/3r^3$ has been used for a spherical cluster. In this case, the interfacial energy is treated as an constant. In Eqs (4.9) and (4.10), d_c is the chemical driving force per unit mole, related to d_c' by $d_c = d_c'/\bar{v}$.

The probability and work of nucleus formation in Eqs (4.5) and (4.6) is the basis for the derivation of the nucleation rate. In the kinetic model of CNT, it is assumed that clusters of n atoms, in atomic configuration E_n grow or dissolve by the addition or loss of a single atom of state E_1. This can be described as a series of bimolecular reactions of the form

$$\begin{aligned} E_{n-1} + E_1 &\underset{k^-(n)}{\overset{k^+(n-1)}{\rightleftarrows}} E_n \\ E_n + E_1 &\underset{k^-(n+1)}{\overset{k^+(n)}{\rightleftarrows}} E_{n+1} \end{aligned} \tag{4.11}$$

were $k^+(n)$ is the rate of atomic attachment to a cluster of size n and $k^-(n)$ is the rate of loss of a single atom from the same cluster. With the above assumptions, the nucleation rate $I(n,t)$ is described as the flux of clusters in size-space per unit volume, given by

$$I(n,t) = N(n,t)k^+(n) - N(n+1)k^-(n+1) \tag{4.12}$$

where $N(n,t)$ is the number of clusters per unit volume of size n at time t, constituting a cluster size distribution. The time evolution of the cluster size distribution is then governed by the difference in the flux (nucleation rate), providing a set of differential equations of the form

$$\frac{\partial N(n,t)}{\partial t} = I(n-1,t) - I(n,t) \tag{4.13}$$

From Eq. (4.12) it becomes apparent that the nucleation rate, in general, is a function of both time and cluster size. The nucleation rate is dependent on the number of existing clusters of size n, thus in the initial stages of the transformation, the nucleation rate is low and increases as the number of clusters evolves. Eventually, steady-state conditions are obtained and the nucleation rate becomes independent of time and cluster size [65, 66]. A well-known analytical expression of the steady-state nucleation rate is given by

$$I^{st} = Zk^+(n^*)N_0 \exp\left(-\frac{W(n^*)}{k_B T}\right) \tag{4.14}$$

where Z is the Zeldovich factor, in its general form expressed as [67]

$$Z = \left[-\frac{1}{2\pi k_B T}\left(\frac{\partial^2 W(n)}{\partial n^2}\right)_{n^*}\right]^{1/2} \tag{4.15}$$

and $k^+(n^*)$ is the atomic attachment rate evaluated at the critical size. N_0 is the initial number density of atoms.

CNT was used in Paper B, C, and E to model nucleation in a Zr-based metallic glass. In Paper B, the evolution of the cluster size distribution was solved numerically under the non-isothermal conditions of the laser powder bed fusion process. Fig. 4.3 shows the numerically computed nucleation rate using Eq. (4.13) under different cooling rates as well as the steady-state nucleation rate given by Eq. (4.14). The high cooling rates in the

LPBF process impair the development of the cluster size distribution and consequently, steady-state conditions are not obtained at lower temperatures. As a result, the transient nucleation rate is several orders of magnitude lower than the rate of steady-state nucleation. The result demonstrates that steady-state conditions are likely, not valid under the rapid heating and cooling conditions involved in the LPBF process.

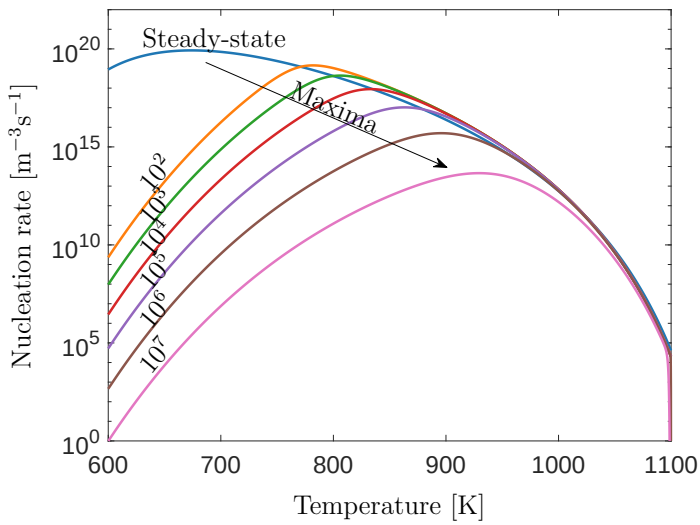

Figure 4.3: Computed transient nucleation rate as a function of temperature for different cooling rates (Ks^{-1}). Increasing the cooling rate results in a slower nucleation rate and a shift in the maximum value to higher temperatures as indicated by the black arrow.

4.2.2 Growth

For a polymorphic transformation, the composition of the particle and the matrix are equal and the growth rate is dictated by the rate of atomic attachment at the interface. The growth is then said to be interface-controlled. Kelton et al. [68] derived an expression for interface-controlled growth based on the differential equations governing nucleation in Eq. (4.13). Following this model, the growth rate is given by

$$v = \frac{16D}{\lambda^2}\left(\frac{3\bar{v}}{4\pi}\right)^{1/3} \sinh\left[\frac{\bar{v}}{2k_BT}\left(\frac{d_c^{poly}}{V_m} - \frac{2\sigma}{r}\right)\right] \tag{4.16}$$

where d_c^{poly} is the chemical driving force for a polymorphic transformation and is described in Section 4.3. This expression was found to agree qualitatively with the polymorphic growth rate from the phase-field model in Paper A. It was used in Paper B and C to model the growth of supercritical clusters. However, the SANS experiments in Paper D indicates

a primary crystallization process in AMZ4, for which the transformation is controlled by diffusion.

As discussed in Section 4.1, for diffusion-controlled growth, the growth rate is governed by the diffusional fluxes at the interface between the crystal and the matrix, which depends on the composition gradient in front of the interface. For a sharp interface approximation, this constitutes a moving boundary value problem, known as the Stefan problem [54, 69]. In general, the diffusion field has to be solved numerically which becomes computationally expensive [67]. However, in the case of spherical particles, approximate solutions of diffusion-controlled growth exist. Such a model was utilized in Paper E and is briefly outlined below.

Chen et al. [70] proposed an approximate solution of the multicomponent growth rate of a spherical particle, which avoids solving the diffusion field by approximating the composition gradient as a linear function of the particle size r. Following this model, the growth rate v is computed from a system of equations in the following form

$$\left(x_i^{\beta\alpha} - x_i^{\alpha\beta}\right) \cdot v = \sum_{j=1}^{n-1} \frac{D_{ij}^{\alpha}\left(x_j^{\alpha} - x_j^{\alpha\beta}\right)}{\xi_j r}, \quad \forall \quad i = 1...n-1 \tag{4.17}$$

where x_i^{α} is the composition in the matrix, $x_i^{\alpha\beta}$ and $x_i^{\beta\alpha}$ are the compositions at the interface on the matrix side and particle side, respectively. n denotes the number of elements in the system, not to be confused with the cluster size in Section 4.2.1. Eq. (4.17) provides $n-1$ equations, one for each independent element in the alloy system. D_{ij}^{α} is the diffusivity matrix of the $n-1$ independent elements and ξ_j is an effective diffusion distance factor, which relates to the effective diffusion distance of the depletion zone through $d_j = \xi_j r$. Eq. (4.17) accounts for cross-diffusivity and unequal diffusivity among the constituent elements. For metallic glasses, the alloying elements have a large atomic size mismatch and unequal diffusivity is expected. These effects were neglected in Paper E, mainly because of the scarcity of reported mobility data of individual elements. Instead, an effective diffusivity coefficient D_{eff}^{α} was used, which was approximated from measured viscosity data.

Assuming equal diffusivity, Eq. (4.17) can be rewritten as

$$v = 2K^2 \frac{D_{eff}^{\alpha}}{r} \tag{4.18}$$

where K is dependent on the matrix supersaturation S. For equal diffusivity, the supersaturation becomes identical for each element i and can be expressed as

$$S = \frac{x_i^{\alpha} - x_i^{\alpha\beta}}{x_i^{\beta\alpha} - x_i^{\alpha\beta}} \tag{4.19}$$

For low supersaturation $S << 1$ then $2K^2 \approx S$ and the well known expression of $v = SD_{eff}^{\alpha}/r$ is obtained. Since crystallization in metallic glasses typically occur far from equilibrium, it is expected that the supersaturation in the matrix can become rather high,

which affects the growth rate. In the case of a high supersaturation $S \leq 1$, the dependence between S and K is given by

$$2K^2 \left[1 - \sqrt{\pi} K \exp\left(K^2\right) \operatorname{erfc}\left(K\right)\right] = S \tag{4.20}$$

Eqs (4.18), (4.19) and (4.20) constitute a moving boundary value problem with unknown boundary conditions, $x_i^{\alpha\beta}$ and $x_i^{\beta\alpha}$, essentially an underdetermined system with $n-1$ equations and $2n-1$ unknown variables. Assume local equilibrium at the interface and the required additional n relationships between $x_i^{\alpha\beta}$ and $x_i^{\beta\alpha}$ are obtained as

$$\mu_i^{\alpha}\left(x_j^{\alpha\beta}\right) = \mu_i^{\beta}\left(x_j^{\beta\alpha}\right) + \frac{2\sigma V_m^{\beta}}{r} \tag{4.21}$$

where μ_i^{α} and μ_i^{β} are the chemical potentials of the bulk matrix and particle phase, respectively. $\mu_i^{\alpha}\left(x_j^{\alpha\beta}\right)$ denote the chemical potential of each element $i = 1...n$ and is a function of the composition of element $j = 1...n$ at the interface. Note that Eq. (4.21) is essentially the same as Eq. (4.3), with the exception of the last term which takes into account the curvature-induced pressure on the spherical particle, known as the Gibbs-Thomson effect [71]. As discussed in Paper A, the Gibbs-Thomson effect is inherently included in the phase-field model. To obtain the growth rate as a function of particle size r, the supersaturation S and the interfacial compositions $x_i^{\alpha\beta}$ and $x_i^{\beta\alpha}$ are computed by solving (4.19) and (4.21) using appropriate thermodynamic models of the matrix and particle phases.

4.3 Thermodynamics

To evaluate the thermodynamic quantities for nucleation and growth, suitable thermodynamic models are required. Both the nucleation rate and the growth rate are strongly dependent on the chemical driving force. The chemical driving force for nucleation in a multicomponent alloy, as discussed in [71], is given by

$$d_c = \max\left(\sum_{i=1}^{n} x_i^{\beta}\mu_i^{\alpha}\left(x_j^{\alpha}\right) - G_m^{\beta}\left(x_j^{\beta}\right)\right) \tag{4.22}$$

where x_i^{β} and G_m^{β} are the composition and the molar Gibbs energy of the particle phase, respectively. The relationship between Eq. (4.22) for nucleation and Eq. (4.21) for growth is further discussed in [71].

In the case of a polymorphic transformation, the composition of the particle and matrix are equal, i.e. $x_i^{\alpha} = x_i^{\beta},\ \forall\ i$, and Eq. (4.22) simply becomes the difference in molar Gibbs energy between the particle and matrix phase, expressed as

$$d_c^{poly} = G_m^{\alpha}(x_i^{\beta}) - G_m^{\beta}(x_i^{\beta}) \tag{4.23}$$

For glass forming alloys, d_c^{poly} is often approximated using specific heat data obtained from DSC measurements [33, 72–74]. The specific heat of the liquid c_p^l and crystalline state c_p^x is fitted as a function of temperature using the Kubaschewki equations [33, 73], given by

$$\begin{aligned} c_p^l(T) &= 3R + aT + bT^{-2} \\ c_p^x(T) &= 3R + cT + dT^2 \end{aligned} \tag{4.24}$$

where a, b, c and d are fitting parameters. The molar Gibbs energy between the liquid and the crystalline state ΔG_m can be calculated by integrating the specific heat w.r.t. temperature to obtain the entropy and the enthalpy, following

$$\begin{aligned} \Delta G_m(T) &= \Delta H_m(T) - T\Delta S_m(T) \\ \Delta H_m(T) &= \Delta H_f - \int_T^{T_m} \Delta c_p^{l-x}(T')dT' \\ \Delta S_m(T) &= \Delta S_f - \int_T^{T_m} \frac{\Delta c_p^{l-x}(T')}{T'}dT' \end{aligned} \tag{4.25}$$

where T_m is the melting temperature, ΔH_f and $\Delta S_f = \Delta H_f/T_m$ are the enthalpy and entropy of fusion, respectively. The thermodynamic model outlined above was used in Paper B and C to describe the driving force for nucleation and growth in AMZ4. The parameters in the Kubaschewski equations were obtained from Heinrich et al. [26] who measured the heat capacity of the liquid and the crystalline state of AMZ4. However, using measurements of specific heat to approximate the driving force involves an inherent limitation. The crystalline state of a multicomponent alloy often consists of multiple coexisting phases of different compositions and structures. In such cases, the value of ΔG_m rather represents the difference in molar Gibbs energy between the mixture of the phases and the liquid, rather than the driving force for nucleation and growth. The difference between d_c, d_c^{poly} and ΔG_m is illustrated in Fig. 4.4.

To calculate the chemical driving force of a phase with a different composition than the matrix (d_c in Fig. 4.4), composition dependent thermodynamic models are required for the evaluation of the chemical potential. The CALPHAD method is a computational framework to model the thermodynamic properties of different phases of an alloy system [75, 76]. In Paper A the molar Gibbs energies were fitted to the CALPHAD assessment of the Cu-Zr system by Gierlotka et al. [77] using polynomials. In Paper E, the thermodynamic database of the Al-Cu-Zr system constructed by Zhou et al. [78] was adopted and fully coupled to the nucleation and growth model. In both assessments, the molar Gibbs energy of the liquid phase G_m^α is described using a substitutional solution model given by

$$G_m^\alpha = \sum_{i=1}^{n} x_i{}^\circ G_i^\alpha + RT\sum_{i=1}^{n} x_i \ln x_i + {}^E G_m^\alpha \tag{4.26}$$

where n is the number of components in the system, G_i^α is the molar Gibbs energy of the pure elements [79] and R is the gas constant. The last term in Eq. (4.26) is the excess

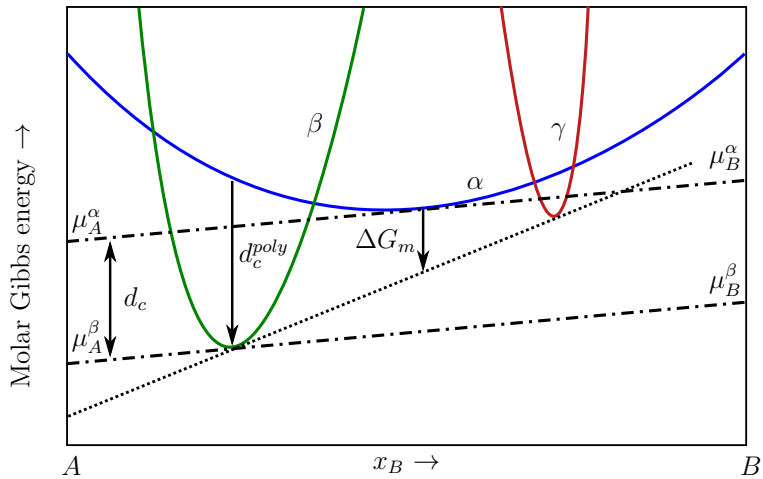

Figure 4.4: Illustration of the driving force d_c of particle phase β (green) for primary crystallization (different composition) and d_c^{poly} for polymorphic crystallization (equal composition) from matrix α (blue) in a binary system. In the case of primary crystallization, the value of d_c is given by the difference in chemical potential between the particle and the matrix. The difference in molar Gibbs energy ΔG_m for transformation of the matrix α to an equilibrium mixture of β and γ (red) phases are included to illustrate that this value is different from the driving force for a specific phase.

Gibbs energy ${}^{E}G_m^\alpha$. For the Al-Cu-Zr system, it is given by

$$ {}^{E}G_m^\alpha = \sum_{i=1}^{n} \sum_{j>i} x_i x_j L_{ij}^\alpha + x_{\mathrm{Al}} x_{\mathrm{Cu}} x_{\mathrm{Zr}} L_{\mathrm{Al,Cu,Zr}}^\alpha \tag{4.27} $$

where L_{ij}^α and $L_{\mathrm{Al,Cu,Zr}}^\alpha$ are the binary and ternary Redlich-Kister polynomials [75, 78]. The first two terms in Eq. (4.26) represent an ideal substitutional solution with non-interacting elements. The excess Gibbs energy in Eq. (4.26) accounts for the negative enthalpies of mixing representing the preferential interaction between the constituent elements [76]. The negative enthalpies of mixing become more negative with increasing undercooling, which stabilizes the liquid phase and result in progressive short-range atomic ordering in the melt [80].

The molar Gibbs energy of an intermetallic crystalline phase is constructed similarly. In the work by Gierlotka et al. [77], the intermetallic phases were modeled as stoichiometric compounds with no solubility. In the work by Zhou et al. [78], the solubility of Al and Cu was included and the intermetallic $(\mathrm{Al,Cu})_p\mathrm{Zr}_q$ phases were modeled as line compounds, with substitutional mixing of Al and Cu on the first sublattice and fixed composition of Zr on the second sublattice. The molar Gibbs energy of formula unit $(\mathrm{Al,Cu})_p\mathrm{Zr}_q$ is expressed

as

$$G_m^\beta = \sum_{i=1}^{2} y_i' G_{\mathrm{i:Zr}}^\beta + pRT \sum_{i=1}^{2} y_i' \ln y_i' + y_{\mathrm{Al}}' y_{\mathrm{Cu}}' L_{\mathrm{Al,Cu:Zr}}^\beta \tag{4.28}$$

where y_i' are the site fractions of $i = \mathrm{Al}, \mathrm{Cu}$ on the first sublattice, $G_{\mathrm{i:Zr}}^\beta$ is the molar Gibbs energy when the first sublattice is occupied by only one element $i = \mathrm{Al}, \mathrm{Cu}$ and $L_{\mathrm{Al,Cu:Zr}}^\beta$ is the binary Redlich-Kister polynomial included in the excess Gibbs energy.

4.4 Interfacial energy

The interfacial energy, σ, defines the work to form the interface between the solid and the liquid phase. It contributes to the growth rate through the Gibbs Thomson effect (see Eqs (4.16) and (4.21)) and to the nucleation rate through the work of nucleus formation. Unfortunately, it is a quantity that is difficult to measure and is often chosen within acceptable known ranges [67, 81]. The interfacial energy depends on the structural and chemical mismatch between the interfacing phases and therefore depends on the thermodynamics of the system.

Several models have been proposed for the solid-liquid interfacial energy [82–85]. One of the more well-known is the model proposed by Turnbull et al. [86]. According to the model, the interfacial energy at the melting point σ_0 can be estimated as

$$\sigma_0 = 0.46 \frac{\Delta H_m^f}{\left(V_m^\beta\right)^{2/3} N_A^{1/3}} \tag{4.29}$$

where ΔH_m^f is the difference in the molar enthalpy of fusion between the solid and liquid phase at the melting point, which can be evaluated from the thermodynamic data.

As discussed in Section 4.1, the capillarity approximation of CNT breaks down at large undercooling where the nucleus no longer shows macroscopic properties. For small clusters, corrections may be introduced for the interfacial energy in CNT. A simple and fairly frequently used correction is the model by Tolman [59, 67], which introduces a size-dependent correction factor of the interfacial energy.

$$\sigma(r) = \frac{\sigma_0}{1 + \frac{2\delta_0}{r}} \tag{4.30}$$

where δ_0 is a characteristic length-scale. According to Kozeschnik et al. [67], a suitable approximation of δ_0 is $\delta_0 = 0.3 r_1$ where r_1 is the distance to the nearest atomic neighbour. The interfacial energy model outlined above was used in Paper E.

In Paper B and C, the model by Mondal et al. [85] was used. The model was chosen because the temperature dependence of the interfacial energy showed a qualitative agreement with molecular dynamics simulations of the Cu-Zr system. The model can be reduced to the following analytical expression

$$\sigma(T) = \left[\frac{P}{\rho\lambda} \frac{3 d_c^{poly}}{32\pi V_m} \left(\Delta G_d^m(T) - \Delta G_d^L(T) \right) \right]^{1/2} \tag{4.31}$$

where $\Delta G_d^m(T)$ is the activation energy for diffusion in the atomic monolayer representing the interface, $\Delta G_d^L(T)$ is the activation energy for diffusion in the liquid. P and ρ are the packing factor and planar atomic density of the crystal, respectively. As seen in Eq. (4.31), the model is more complex than Turnbull's model and depends on the activation energy of diffusion through the interface, as well as packing constraints, of the crystal. The inclusion of parameters that depend on the atomic packing in Eq. (4.31) shows a similarity to the size-correction factor in Eq. (4.30), where δ_0 is associated with the inter-atomic distances in the material. In Paper B, the values of $\Delta G_d^m(T)$ and P/ρ were fitted to a measured TTT-diagram by computing the crystalline volume fraction under the assumption of constant nucleation and growth rates.

4.5 Application to laser powder bed fusion

The nucleation model outlined in Section 4.2.1 together with the polymorphic growth model in Eq. (4.16) was used in Paper B and C to simulate crystallization during laser processing of AMZ4. Finite element simulations of the transient thermal field during LPBF processing of AMZ4 were considered. The temperature history experienced by a material point in the vicinity of the melt pool for a laser power of 105 W is shown in Fig. 2.5. The computed volume fraction in the same material point as a function of time for different laser powers using the transient nucleation model is shown in Fig. 4.5 a). The result shows an important aspect of the crystallization process during LPBF processing. The volume fraction is initially low and no substantial crystallization occurs during the deposition of the first layer. The cooling rate is simply too high ($\approx 10^6$ Ks^{-1}) to cause any significant crystallization. However, nuclei are formed upon cooling and as the next layer is deposited, the material becomes reheated and the volume fraction increases rapidly because of the growth of nuclei formed during the previous cycle. For each consecutive reheating cycle, more nuclei form and grow, increasing the volume fraction further. The result suggests that the main crystallization events occur during reheating of the material in the LPBF process.

The effect of changing the laser power on the crystalline volume fraction is shown in Fig. 4.5 b). At an increasing laser power, the material absorbs more energy and the temperature field around the melt pool becomes higher. The accumulated energy requires a longer time to dissipate and exposes the material to higher nucleation and growth rates for a longer duration, resulting in a higher crystalline volume fraction as the laser power is increased.

The effect of multiple reheating was further investigated in Paper C. Simulations of multiple laser remelting scans in a single track were performed to study crystallization in the vicinity of the melt pool. Figs 4.6 a) and 4.6 b) show the number density and mean radius of crystals for each consecutive scan as a function of the distance from the melt pool, respectively. A trend can be observed where repeated remelting results in an increased number density of larger crystals in the heat affected zone (HAZ). The laser heat source causes a thermal gradient that gives rise to different temperature histories in the

HAZ. Consequently, crystals form and grow at various rates depending on the location in the HAZ, resulting in a gradient of crystal number density and crystal size. The results were found to agree qualitatively with microscopy images of the HAZ in Paper B.

The results from the SANS experiments from Paper D indicate a primary crystallization process where the rate of transformation is controlled by diffusion. For this reason, a diffusion-controlled growth model was adopted in Paper E to predict the growth rate during primary crystallization in AMZ4. The growth model is also expected to have a pronounced effect on the rate of crystallization in LPBF as the major crystallization events occur upon reheating.

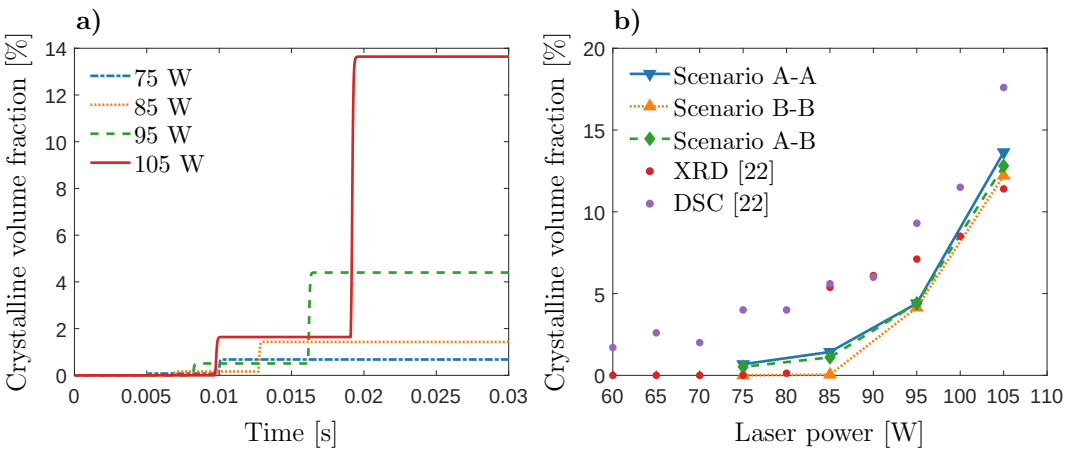

Figure 4.5: Computed crystalline volume fraction for different laser power using the transient nucleation model in Paper B. a) As a function of time. The volume fraction for 105 W correspond to the temperature history shown in Fig. 2.5. b) Final crystalline volume fraction for different scanning scenarios as a function of laser power. Estimations of crystalline volume fraction using X-ray diffraction and DSC from [22] is included for comparison.

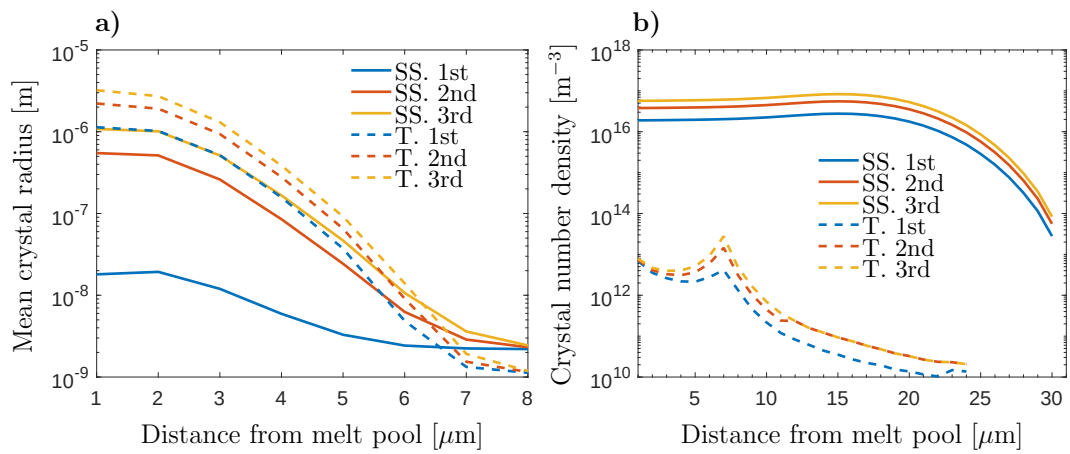

Figure 4.6: Computed crystallization using steady-state (SS.) and transient nucleation (T.) in the heat affected zone from Paper C: a) Mean crystal radius as a function of the distance from the melt pool for each consecutive laser scan (1st, 2nd and 3rd). b) Crystal number density as a function of the distance from the melt pool for each consecutive laser scan (1st, 2nd and 3rd). Gradients in mean crystal size and crystal number density are observed, caused by the thermal gradient in the HAZ.

Chapter 5

Summary and future perspectives

Attributed to the amorphous atomic structure, metallic glasses show exceptional mechanical and magnetic properties that are desired in applications for the automotive, aerospace, and biomedical industries. Additive manufacturing by laser powder bed fusion (LPBF) is a promising technique for the production of large metallic glass components. Despite the high cooling rates inherent to the process, control of crystallization is still an issue and the interplay between the complex thermal process and the formation and growth of crystals is not fully understood. The work presented in this thesis aims at advancing the knowledge of the crystallization process during the non-isothermal processing of a bulk metallic glass, with a special emphasis on additive manufacturing.

As part of the thesis, numerical simulations and experimental analyses related to the formation and growth of crystals in a Zr-based bulk metallic glass have been presented. The experimental study using small angle neutron scattering shows that crystals formed at a higher rate in a Zr-based processed by LPBF, as a result of the increased oxygen content in the feedstock powder material. The study also identified the crystallization mechanisms in the material as rapid nucleation followed by diffusion-controlled growth.

The numerical simulations are based on phase-field and classical nucleation and growth theory, which were developed to study the nucleation, growth, and dissolution of crystals in a Zr-based metallic glass. The models have been used to predict transformation diagrams but also to simulate the crystallization process during LPBF by utilizing thermal finite element simulations of the laser-material interaction. The results demonstrate that classical nucleation and growth theory is suitable for the prediction of crystallization during the non-isothermal process involved in additive manufacturing by LPBF.

5.1 Future perspectives

Metallic glass is essentially a liquid that has fallen out of equilibrium. The thermodynamic models used in this thesis assume that the liquid is in internal equilibrium and the models do not consider the glass transition. The connection between the deviation from internal equilibrium upon glass formation and the kinetic events of crystallization is still unclear.

Recent work has integrated the structural relaxation of the glassy state with classical nucleation theory and the result indicates that the deviations from internal equilibrium can have a large effect on the work of nucleus formation and therefore also the nucleation rate [87, 88]. The development of thermodynamic models of the glass transition is also an exciting field of research in the CALPHAD community [89, 90]. Metallic glasses produced by laser powder bed fusion may show variations in structural relaxation in the component because of the varying cooling rates and thermal gradients [91].

In terms of oxygen, it would be interesting to apply the model in Paper E to a thermodynamic description involving Cu-Zr-O. Such a model could be used to model the conditions for the formation of oxygen-enriched phases depending on the oxygen content in the material. Modeling of heterogeneous nucleation would also be an interesting topic related to the oxygen content since the stable phases are believed to form heterogeneously on the oxygen-enriched crystals. Models of heterogeneous nucleation are likely useful for other industrial glass forming alloys where impurities are of importance.

From a broader perspective, the models presented in this thesis can be used to predict the formation and growth of crystals during non-isothermal processing of BMGs. In combination with thermal simulations of the moving laser heat source in LPBF, such models can be used to understand where and when crystallization occurs depending on the chosen process parameters and scanning strategies. The coupling of crystallization models to CALPHAD databases could be used to predict transformation diagrams of different crystalline phases and aid the development of new alloys with phase selection tailored for additive manufacturing. In most cases, the purpose would be to avoid crystallization to obtain the amorphous material properties. However, for some BMGs, partial crystallization has shown to be favorable as it combines the properties of the amorphous material with that of crystalline particles, forming a BMG-crystalline composite [92, 93]. For example, the ductile B2 CuZr crystalline phase may improve the ductility of brittle Zr-based metallic glasses [94] and the formation of nanometer sized α-Fe(Si) crystallites in a Fe-based metallic glass may improve the soft magnetic properties [95], leading to lower energy losses in electrical applications. Additive manufacturing could be used to locally tailor such properties by controlling the thermal gradients and temperature histories that give rise to different crystal number densities and sizes at different locations in the material. In combination with the ability to design complex geometries, tailored components with unique properties may be envisaged for the future. For example, structurally optimized lightweight components or magnetic components with geometrical and microstructural tailored magnetic fields [96, 97]. The work presented in this thesis takes a step in the development of BMG-crystalline composites with material properties tailored by additive manufacturing.

Summary of appended papers

Paper A: A methodology combining phase-field and classical nucleation theory is developed to model the process of nucleation and growth in a glass forming system. The methodology is applied to evaluate the crystallization of the $CuZr_2$ and $Cu_{10}Zr_7$ intermetallic phases in the Cu-Zr system and permit the construction of TTT-diagrams. The influence of composition gradients is shown to lower the work of formation and cause diffusion-limited growth of the $Cu_{10}Zr_7$ phase from a matrix of neighbouring composition $Cu_{64}Zr_{36}$, resulting in a lower nucleation and growth rate. Furthermore, the work of formation and growth rates obtained from the phase-field model are compared with analytical expression of nucleation and growth from the classical theory.

Paper B: A numerical model based on classical nucleation theory (CNT) is developed to model crystallization of a Zr-based bulk metallic glass during processing by selective laser melting. The CNT model is calibrated to a time-temperature-transformation diagram, obtained from differential scanning calorimetry measurements of crystallization. Thermal finite element is used to model the temperature field resulting from the laser-material interaction. It is demonstrated that the high heating and cooling rates in SLM may cause the break down of the steady-state assumption of nucleation. The crystalline volume fraction in the heat affected zone is compared to experimental estimates and a good correlation between experiment and simulation is observed.

Paper C: The model developed in Paper B is used to investigate the crystallization during multiple laser remelting of a Zr-based metallic glass. The simulation results are compared to scanning electron microscopy (SEM) imaging of the crystallized heat affected zone resulting from multiple laser scans on an metallic glass substrate. Repeated remelting results in increased crystallization in the heat affected zone. The width of the crystalline zone is of comparable size in the SEM images and simulations. A gradient of crystal size and particle density is predicted by the model in agreement with experimental observations.

Paper D: The crystallization mechanisms during low temperature annealing of a Zr-based bulk metallic glass produced by suction casting and laser powder bed fusion (LPBF) were investigated using *in-situ* small angle neutron scattering (SANS), *ex-situ* X-ray diffraction and scanning electron microscopy. It is shown that the phase separation proceed at a smaller characteristic length scale in the LPBF processed material. Analysis of the

SANS data reveals that both materials crystallize through rapid nucleation followed by diffusion limited growth. The higher nucleation rate and smaller particle size distribution is attributed to the elevated oxygen content of the LPBF processed samples, which reduces the energy barrier to nucleation.

Paper E: A modeling methodology of nucleation, growth and dissolution of crystals in a multicomponent glass forming system is established. The numerical model solves the evolution of the crystal size distribution by making use of classical nucleation theory and a multicomponent diffusion-controlled growth model. The composition and temperature dependent thermodynamic properties are obtained by fully couple the model to a CALPHAD database. The Al-Cu-Zr system is selected as a demonstrator and the crystallization of intermetallic $(\mathrm{Al}, \mathrm{Cu})_{\mathrm{p}}\mathrm{Zr}_{\mathrm{q}}$ phases is simulated under isothermal as well as rapid heating and cooling conditions ($10^{-1} - 10^{6}$ Ks^{-1}). The model predicts the asymmetry in the critical heating/cooling rate and the role of formation, growth and dissolution of crystals during cyclic heating/cooling. The predicted transformation diagrams are compared to experimental data over a wide temperature range.

References

[1] W. Klement, R. H. Willens, and P. Duwez. Non-crystalline structure in solidified Gold-Silicon alloys. *Nature*, 187(4740):869–870, 1960. ISSN 00280836. doi: 10.1038/187869b0.

[2] J. F. Löffler. Bulk metallic glasses. *Intermetallics*, 11:529–540, 2003. doi: 10.1016/S0966-9795(03)00046-3.

[3] M. Telford. The case for bulk metallic glass. *Materials Today*, 7(3):36–43, 2004. ISSN 13697021. doi: 10.1016/S1369-7021(04)00124-5.

[4] A. Inoue. Bulk Glassy Alloys: Historical Development and Current Research. *Engineering*, 1(2):185–191, 2015. ISSN 20958099. doi: 10.15302/J-ENG-2015038.

[5] H.W. Kui, A.L. Greer, and D. Turnbull. Formation of bulk metallic glass by fluxing. *Applied Physics Letters*, 45(6):615–616, 1984. doi: 10.1063/1.95330.

[6] A. Inoue, T. Zhang, and T. Masumoto. Al-La-Ni Amorphous Alloys with a Wide Supercooled Liquid Region. *Materials Transactions*, 30(12):965–972, 1989. doi: 10.2320/matertrans1989.31.104.

[7] T. Zhang, A. Inoue, and T. Masumoto. Amorphous Zr-Al-TM (TM=Co,Ni,Cu) Alloys with Significant Supercooled Liquid Region of Over 100K. *Materials Transactions*, 32 (11):1005–1010, 1991. doi: 10.2320/matertrans1989.32.1005.

[8] A. Inoue, A. Kato, T. Zhang, S. G. Kim, and T. Masumoto. Mg-Cu-Y Amorphous Alloys with High Mechanical Strengths Produced by a Metallic Mold Casting Method. *Materials Transactions*, 32(7):609–616, 1991. doi: 10.2320/matertrans1989.32.609.

[9] A. Peker and W. L. Johnson. A highly processable metallic glass: $Zr_{41.2}T_{13.8}Cu_{12.5}Ni_{10.0}Be_{22.5}$. *Applied Physics Letters*, 63:2342–2344, 1993. doi: 10.1063/1.110520.

[10] A. Inoue, W. Zhang, T. Zhang, and K. Kurosaka. Cu-Based Bulk Glassy Alloys with Good Mechanical Properties in Cu-Zr-Hf-Ti System. *Materials Transactions*, 42(8): 1805–1812, 2001. doi: 10.2320/matertrans.42.1805.

[11] V. Ponnambalam, S. J. Poon, and G. J. Shiflet. Fe-based bulk metallic glasses with diameter thickness larger than one centimeter. *Materials Research and Society*, 19(5): 1320–1323, 2004. doi: 10.1557/JMR.2004.0176.

[12] C. Chang, B. Shen, and A. Inoue. Co–Fe–B–Si–Nb bulk glassy alloys with superhigh strength and extremely low magnetostriction. *Applied Physics Letters*, 88:011901, 2006. doi: 10.1063/1.2159107.

[13] K. Amiya and A. Inoue. Fe-(Cr ,Mo)-(C,B)-Tm Bulk Metallic Glasses with High Strength and High Glass-Forming Ability. *Materials Transactions*, 47(6):1615–1618, 2006. doi: 10.2320/matertrans.47.1615.

[14] S. L. Zhu, X. M. Wang, and A. Inoue. Glass-forming ability and mechanical properties of Ti-based bulk glassy alloys with large diameters of up to 1 cm. *Intermetallics*, 16: 1031–1035, 2008. doi: 10.1016/j.intermet.2008.05.006.

[15] Z. Yuqiao, N. Nishiyama, and A. Inoue. Development of Ni-Pd-P-B Bulk Metallic Glasses with High Glass-Forming Ability. *Materials Transactions*, 50(6):1243–1246, 2009. doi: 10.2320/matertrans.ME200834.

[16] A. Inoue, N. Nishiyama, and H. Kimura. Preparation and Thermal stability of Bulk Amorphous $Pd_{40}Cu_{30}Ni_{10}P_{20}$ Alloy Cylinder of 72 mm in Diameter. *Materials Transactions*, 38(2):179–183, 1997. doi: 10.2320/matertrans1989.38.179.

[17] S. Pauly, L. Löber, R. Petters, M. Stoica, S. Scudino, U. Kühn, and J. Eckert. Processing metallic glasses by selective laser melting. *Materials Today*, 16:37–41, 2013. doi: 10.1016/j.mattod.2013.01.018.

[18] X. P. Li, C. W. Kang, H. Huang, L. C. Zhang, and T. B. Sercombe. Selective laser melting of an $Al_{86}Ni_6Y_{4.5}Co_2La_{1.5}$ metallic glass: Processing, microstructure evolution and mechanical properties. *Materials Science and Engineering A*, 606:370–379, 2014. ISSN 09215093. doi: 10.1016/j.msea.2014.03.097.

[19] Z. Mahbooba, L. Thorsson, M. Unosson, P. Skoglund, H. West, T. Horn, C. Rock, E. Vogli, and O. Harrysson. Additive manufacturing of an iron-based bulk metallic glass larger than the critical casting thickness. *Applied Materials Today*, 11:264–269, 2018. ISSN 23529407. doi: 10.1016/j.apmt.2018.02.011.

[20] L. Deng, S. Wang, P. Wang, U. Kühn, and S. Pauly. Selective laser melting of a Ti-based bulk metallic glass. *Materials Letters*, 212:346–349, 2018. ISSN 18734979. doi: 10.1016/j.matlet.2017.10.130.

[21] V. Pacheco, D. Karlsson, J. J. Marattukalam, M. Stolpe, B. Hjörvarsson, U. Jansson, and M. Sahlberg. Thermal stability and crystallization of a Zr-based metallic glass produced by suction casting and selective laser melting. *Journal of Alloys and Compounds*, 825:153995, 2020. ISSN 09258388. doi: 10.1016/j.jallcom.2020.153995.

[22] J. J. Marattukalam, V. Pacheco, D. Karlsson, L. Riekehr, J. Lindwall, F. Forsberg, U. Jansson, M. Sahlberg, and B. Hjörvarsson. Development of process parameters for selective laser melting of a Zr-based bulk metallic glass. *Additive Manufacturing*, 33: 101124, 2020. ISSN 22148604. doi: 10.1016/j.addma.2020.101124.

[23] P. Bordeenithikasem, M. Stolpe, A. Elsen, and D. C. Hofmann. Glass forming ability, flexural strength, and wear properties of additively manufactured Zr-based bulk metallic glasses produced through laser powder bed fusion. *Additive Manufacturing*, 21:312–317, 2018. ISSN 22148604. doi: 10.1016/j.addma.2018.03.023.

[24] H. Liu, Q. Jiang, J. Huo, Y. Zhang, W. Yang, and X. Li. Crystallization in additive manufacturing of metallic glasses : A review. *Additive Manufacturing*, 36:101568, 2020. ISSN 2214-8604. doi: 10.1016/j.addma.2020.101568.

[25] N. Sohrabi, J. Jhabvala, and R. E. Log. Additive Manufacturing of Bulk Metallic Glasses — Process , Challenges and Properties: A Review. *Metals*, 11:1279, 2021. doi: 10.3390/met11081279.

[26] J. Heinrich, R. Busch, and B. Nonnenmacher. Processing of a bulk metallic glass forming alloy based on industrial grade Zr. *Intermetallics*, 25:1–4, 2012. ISSN 09669795. doi: 10.1016/j.intermet.2012.02.011.

[27] Heraeus AMLOY Technologies. Material datasheet: AMLOY-ZR01. `https://www.heraeus.com/media/media/group/media_group/products/amorphous_metals/datasheets_1/Datasheet_AMLOY-ZR01~2.pdf`.

[28] D. B. Miracle, T. Egami, K. M. Flores, and K. F. Kelton. Structural aspects of metallic glasses. *Mrs bulletin*, 32:629–634, 2007. doi: 10.1557/mrs2007.124.

[29] X. Yue, A. Inoue, C-T. Liu, and C. Fan. The Development of Structure Model in Metallic Glasses. *Materials Research*, 20(2):326–338, 2017. ISSN 1980-5373. doi: 10.1590/1980-5373-mr-2016-0318.

[30] C. Suryanarayana and A. Inoue. *Bulk Metallic Glasses*. CRC Press, Boca Raton, FL, 1st ed. edition, 2011. ISBN 9781444310085.

[31] M. F. Ashby and A. L. Greer. Metallic glasses as structural materials. *Scripta Materialia*, 54(3):321–326, 2006. ISSN 13596462. doi: 10.1016/j.scriptamat.2005.09.051.

[32] J. C. Dyre. The glass transition and elastic models of glass-forming liquids. *Rev. Mod. Phys.*, 78:953–972, 2006. doi: 10.1103/RevModPhys.78.953.

[33] Z. J. Evenson. *On the thermodynamic and kinetic properties of bulk glass forming metallic systems*. Doctorial thesis, Universität des Saarlandes, 2012.

[34] B. Ruta, E. Pineda, and Z. Evenson. Relaxation processes and physical aging in metallic glasses. *Journal of Physics Condensed Matter*, 29(50), 2017. ISSN 1361648X. doi: 10.1088/1361-648X/aa9964.

[35] D. Turnbull. Under What Conditions Can A Glass Be Formed? *Contemporary Physics*, 10(5), 1969. ISSN 13665812. doi: 10.1080/00107516908204405.

[36] A. Inoue, D. Kawase, and A. P. Tsai. Stability and transformation to crystalline phases of amorphous Zr-Al-Cu alloys with significant supercooled liquid region. *Materials Science and Engineering A*, 178:255–263, 1994.

[37] A. Inoue. Stabilization of metallic supercooled liquid and bulk amorphous alloys. *Acta Materialia*, 48(1):279–306, 2000. ISSN 13596454. doi: 10.1016/S1359-6454(99)00300-6.

[38] Q. Zheng, Y. Zhang, M. Montazerian, O. Gulbiten, J. C. Mauro, E. D. Zanotto, and Y. Yue. Understanding Glass through Differential Scanning Calorimetry. *Chemical Reviews*, 119(13):7848–7939, 2019. ISSN 15206890. doi: 10.1021/acs.chemrev.8b00510.

[39] C. F. Holder and R. E. Schaak. Tutorial on Powder X-ray Diffraction for Characterizing Nanoscale Materials. *ACS Nano*, 13(7):7359–7365, 2019. ISSN 1936086X. doi: 10.1021/acsnano.9b05157.

[40] J. F. Loffler, S. Bossuyt, S. C. Glade, W. L. Johnson, W. Wagner, and P. Thiyagarajan. Crystallization of bulk amorphous Zr–Ti(Nb)–Cu–Ni–Al. *Applied Physics Letters*, 77 (4):525, 2000. ISSN 00036951. doi: 10.1063/1.127032.

[41] I. Martin, T. Ohkubo, M. Ohnuma, B. Deconihout, and K. Hono. Nanocrystallization of $Zr_{41.2}Ti_{13.8}Cu_{12.5}Ni_{10.0}Be_{22.5}$ metallic glass. *Acta Materialia*, 52(15):4427–4435, 2004. ISSN 13596454. doi: 10.1016/j.actamat.2004.05.038.

[42] K. Kajiwara, M. Ohnuma, T. Ohkubo, D. H. Ping, and K. Hono. APFIM/TEM/SAXS studies of early stage crystallization of a $Zr_{52.5}Cu_{17.9}Ni_{14.6}Al_{10}Ti_5$ metallic glass. *Materials Science and Engineering A*, 375-377:738–743, 2004. ISSN 09215093. doi: 10.1016/j.msea.2003.10.087.

[43] X. Wu, S. Lan, X. Wei, J. Zhou, Z. Lu, J. D. Almer, and X. L. Wang. Elucidating the nature of crystallization kinetics in $Zr_{46}Cu_{46}Al_8$ metallic glass through simultaneous WAXS/SAXS measurements. *Applied Physics Letters*, 114(21):211903, 2019. ISSN 00036951. doi: 10.1063/1.5088984.

[44] U. Köster and U. Herold. Crystallization of metallic glasses. In H-J. Güntherodt and H. Beck, editors, *Glassy Metals I*, pages 225–259. 1981. doi: 10.1007/3540104402_10.

[45] D. H. Kim, W. T. Kim, E. S. Park, N. Mattern, and J. Eckert. Phase separation in metallic glasses. *Progress in Materials Science*, 58(8):1103–1172, 2013. ISSN 00796425. doi: 10.1016/j.pmatsci.2013.04.002.

[46] D. Herzog, V. Seyda, E. Wycisk, and C. Emmelmann. Additive manufacturing of metals. *Acta Materialia*, 117:371–392, 2016. ISSN 13596454. doi: 10.1016/j.actamat.2016.07.019.

[47] E. Williams and N. Lavery. Laser processing of bulk metallic glass: A review. *Journal of Materials Processing Technology*, 247(March):73–91, 2017. ISSN 09240136. doi: 10.1016/j.jmatprotec.2017.03.034.

[48] X. P. Li, M. P. Roberts, S. O'Keeffe, and T. B. Sercombe. Selective laser melting of Zr-based bulk metallic glasses: Processing, microstructure and mechanical properties. *Materials and Design*, 112:217–226, 2016. ISSN 18734197. doi: 10.1016/j.matdes.2016.09.071.

[49] Y. B. Melnichenko. *Small-angle scattering from confined and interfacial fluids: Applications to energy storage and environmental science*. 2015. ISBN 9783319011042. doi: 10.1007/978-3-319-01104-2.

[50] O. Arnold, J. C. Bilheux, J. M. Borreguero, A. Buts, S. I. Campbell, L. Chapon, M. Doucet, N. Draper, R. Ferraz Leal, M. A. Gigg, V. E. Lynch, A. Markvardsen, D. J. Mikkelson, R. L. Mikkelson, R. Miller, K. Palmen, P. Parker, G. Passos, T. G. Perring, P. F. Peterson, S. Ren, M. A. Reuter, A. T. Savici, J. W. Taylor, R. J. Taylor, R. Tolchenov, W. Zhou, and J. Zikovsky. Mantid - Data analysis and visualization package for neutron scattering and μ SR experiments. *Nuclear Instruments and Methods in Physics Research A*, 764:156–166, 2014. ISSN 01689002. doi: 10.1016/j.nima.2014.07.029.

[51] A. Guinier and G. Fournet. *Small-angle scattering of X-rays*, volume 19. John Wiley & Sons, Inc., 1st edition, 1955. doi: 10.1002/pol.1956.120199326.

[52] S. Haas, J. Andersson, M. Fisk, J. S. Park, and U. Lienert. Correlation of precipitate evolution with Vickers hardness in Haynes® 282® superalloy: In-situ high-energy SAXS/WAXS investigation. *Materials Science and Engineering A*, 711:250–258, 2018. ISSN 09215093. doi: 10.1016/j.msea.2017.11.035.

[53] R. B. Bergmann and A. Bill. On the origin of logarithmic-normal distributions: An analytical derivation, and its application to nucleation and growth processes. *Journal of Crystal Growth*, 310(13):3135–3138, 2008. ISSN 00220248. doi: 10.1016/j.jcrysgro.2008.03.034.

[54] W. J. Boettinger, J. A. Warren, C. Beckermann, and A. Karma. Phase-Field Simulation of Solidification. *Annual Review of Materials Research*, 32(1):163–194, 2002. ISSN 1531-7331. doi: 10.1146/annurev.matsci.32.101901.155803.

[55] R. Kobayashi. Modeling and numerical simulations of dendritic crystal growth. *Physica D*, 63:410–423, 1993. ISSN 01672789. doi: 10.1016/0167-2789(93)90120-P.

[56] A. Karma and W-J. Rappel. Quantitative phase-field modeling of dendritic growth in two and three dimensions. *Physical Review E*, 57(4):4323–4349, 1998. ISSN 1063-651X. doi: 10.1103/PhysRevE.57.4323.

[57] T. Takaki, Y. Hisakuni, T. Hirouchi, A. Yamanaka, and Y. Tomita. Multi-phase-field simulations for dynamic recrystallization. *Computational Materials Science*, 45(4): 881–888, 2009. ISSN 09270256. doi: 10.1016/j.commatsci.2008.12.009.

[58] Y. Wang, D. Banerjee, C. C. Su, and A. G. Khachaturyan. Field kinetic model and computer simulation of precipitation of L12 ordered intermetallics from f.c.c. solid solution. *Acta Materialia*, 46(9):2983–3001, 1998. ISSN 13596454. doi: 10.1016/S1359-6454(98)00015-9.

[59] L. Gránásy, G. I. Tóth, J. A. Warren, F. Podmaniczky, G. Tegze, L. Rátkai, and T. Pusztai. Phase-field modeling of crystal nucleation in undercooled liquids – A review. *Progress in Materials Science*, 106(October 2018):100569, 2019. ISSN 00796425. doi: 10.1016/j.pmatsci.2019.05.002.

[60] N. Moelans, B. Blanpain, and P. Wollants. An introduction to phase-field modeling of microstructure evolution. *Calphad: Computer Coupling of Phase Diagrams and Thermochemistry*, 32(2):268–294, 2008. ISSN 03645916. doi: 10.1016/j.calphad.2007.11.003.

[61] S. G. Kim, W. T. Kim, and T. Suzuki. Phase-field model for binary alloys. *Physical review. E, Statistical physics, plasmas, fluids, and related interdisciplinary topics*, 60 (6 Pt B):7186–7197, 1999. ISSN 1063-651X. doi: 10.1103/PhysRevE.60.7186.

[62] P. Hohenberg and B. Halperin. Theory of dynamic critical phenomena. *Reviews of Modern Physics*, 49(3):435–479, 1977. ISSN 0034-6861. doi: 10.1103/RevModPhys.49.435.

[63] S. G. Kim. A phase-field model with antitrapping current for multicomponent alloys with arbitrary thermodynamic properties. *Acta Materialia*, 55(13):4391–4399, 2007. ISSN 13596454. doi: 10.1016/j.actamat.2007.04.004.

[64] K. F. Kelton and A. L. Greer. *Nucleation in condensed matter: applications in materials and biology*. Pergamon, Oxford, 1st edition, 2010. ISBN 1470-1804. doi: 10.1016/S1470-1804(09)01515-6.

[65] K. F. Kelton, A. L. Greer, and C. V. Thompson. Transient nucleation in condensed systems. *The Journal of Chemical Physics*, 79(12):6261–6276, 1983. ISSN 00219606. doi: 10.1063/1.445731.

[66] Y. T. Shen, T. H. Kim, A. K. Gangopadhyay, and K. F. Kelton. Icosahedral order, frustration, and the glass transition: Evidence from time-dependent nucleation and supercooled liquid structure studies. *Physical Review Letters*, 102(5):6–9, 2009. ISSN 00319007. doi: 10.1103/PhysRevLett.102.057801.

[67] E. Kozeschnik. *Modeling Solid-State Precipitation*. Momentum press, 2012. doi: 10.5643/9781606500644.

[68] K. F. Kelton and A.L. Greer. Transient nucleation effects in glass formation. *Journal of Non-Crystalline Solids*, 79:295–309, 1986. doi: 10.1016/0022-3093(86)90229-2.

[69] I. Steinbach. Phase-field models in materials science. *Modelling and Simulation in Materials Science and Engineering*, 17(7):073001, 2009. ISSN 0965-0393. doi: 10.1088/0965-0393/17/7/073001.

[70] Q. Chen, J. Jeppsson, and J. Ågren. Analytical treatment of diffusion during precipitate growth in multicomponent systems. *Acta Materialia*, 56(8):1890–1896, 2008. ISSN 13596454. doi: 10.1016/j.actamat.2007.12.037.

[71] B. Rheingans and E. J. Mittemeijer. Modelling precipitation kinetics: Evaluation of the thermodynamics of nucleation and growth. *Calphad: Computer Coupling of Phase Diagrams and Thermochemistry*, 50:49–58, 2015. ISSN 03645916. doi: 10.1016/j.calphad.2015.04.013.

[72] R. Busch, J. Schroers, and W. H. Wang. Thermodynamics and Kinetics of Bulk Metallic Glass. 32(8):620–623, 2007. doi: 10.1557/mrs2007.122.

[73] W. Hembree. *High temperature rheology of Zr-based bulk metallic glass forming liquids*. Doctorial thesis, Universität des Saarlandes, 2015.

[74] J. Schawe, S. Pogatscher, and J. F. Löffler. Thermodynamics of polymorphism in a bulk metallic glass: Heat capacity measurements by fast differential scanning calorimetry. *Thermochimica Acta*, 685:178518, 2020. ISSN 00406031. doi: 10.1016/j.tca.2020.178518.

[75] H. L. Lukas, S. G. Fries, and B. Sundman. *Computational thermodynamics: The Calphad method*. 2007. ISBN 9780511804137. doi: 10.1017/CBO9780511804137.

[76] M. Palumbo and L. Battezzati. Thermodynamics and kinetics of metallic amorphous phases in the framework of the CALPHAD approach. *Calphad: Computer Coupling of Phase Diagrams and Thermochemistry*, 32(2):295–314, 2008. ISSN 03645916. doi: 10.1016/j.calphad.2007.12.002.

[77] W. Gierlotka, K. C. Zhang, and Y. P. Chang. Thermodynamic description of the binary Cu-Zr system. *Journal of Alloys and Compounds*, 509(33):8313–8318, 2011. ISSN 09258388. doi: 10.1016/j.jallcom.2011.04.141.

[78] C. Zhou, C. Guo, C. Li, and Z. Du. Thermodynamic assessment of the phase equilibria and prediction of glass-forming ability of the Al–Cu–Zr system. *Journal of Non-Crystalline Solids*, 461:47–60, 2017. ISSN 00223093. doi: 10.1016/j.jnoncrysol.2016.09.031.

[79] A. T. Dinsdale. SGTE DATA FOR PURE ELEMENTS. *Calphad: Computer Coupling of Phase Diagrams and Thermochemistry*, 15(4):317–425, 1991. doi: 10.1016/0364-5916(91)90030-N.

[80] R. Bormann. Thermodynamics of undercooled liquids and its application to amorphous phase formation. *Materials Science and Engineering A*, 178(1-2):55–60, 1994. ISSN 09215093. doi: 10.1016/0921-5093(94)90518-5.

[81] Q. Du, W. J. Poole, and M. A. Wells. A mathematical model coupled to CALPHAD to predict precipitation kinetics for multicomponent aluminum alloys. *Acta Materialia*, 60(9):3830–3839, 2012. ISSN 13596454. doi: 10.1016/j.actamat.2012.02.050.

[82] D. R. Uhlmann. Crystallization and Melting in Glass-Forming Systems. In *Kinetics of Reactions in Ionic Systems*, pages 172–197, Boston, MA, 1969. Springer US. ISBN 978-1-4899-6461-8.

[83] F. Spaepen and R. B Meyer. The surface tension in a structural model for the solid-liquid interface. *Scripta Metallurgica*, 10(3):257–263, 1976. ISSN 0036-9748. doi: 10.1016/0036-9748(76)90374-4.

[84] L. Gránásy. Quantitative analysis of the classical nucleation theory on glass- forming alloys. *Journal of Non-Crystalline Solids*, 158:514–518, 1993. doi: 10.1016/0022-3093(93)90010-U.

[85] K. Mondal, A. Kumar, G. Gupta, and B. S. Murty. Temperature and structure dependency of solid-liquid interfacial energy. *Acta Materialia*, 57(11):3422–3430, 2009. ISSN 13596454. doi: 10.1016/j.actamat.2009.03.051.

[86] D. Turnbull. Correlation of Liquid-Solid Interfacial Energies Calculated from Supercooling of Small Droplets. *The Journal of Chemical Physics*, 18(5):769–769, 1950. ISSN 0021-9606. doi: 10.1063/1.1747766.

[87] J. Schmelzer, T. V. Tropin, V. M. Fokin, A. S. Abyzov, and E. D. Zanotto. Effects of glass transition and structural relaxation on crystal nucleation: Theoretical description and model analysis. *Entropy*, 22(10):1–36, 2020. ISSN 10994300. doi: 10.3390/e22101098.

[88] V. M. Fokin, A. S. Abyzov, N. S. Yuritsyn, J. Schmelzer, and E. D. Zanotto. Effect of structural relaxation on crystal nucleation in glasses. *Acta Materialia*, 203:116472, 2021. ISSN 13596454. doi: 10.1016/j.actamat.2020.11.014.

[89] C. A. Becker, J. Ågren, M. Baricco, Q. Chen, S. A. Decterov, U. R. Kattner, J. H. Perepezko, G. R. Pottlacher, and M. Selleby. Thermodynamic modelling of liquids: CALPHAD approaches and contributions from statistical physics. *Physica Status Solidi (B) Basic Research*, 251(1):33–52, 2014. ISSN 15213951. doi: 10.1002/pssb.201350149.

[90] P. Benigni. CALPHAD modeling of the glass transition for a pure substance, coupling thermodynamics and relaxation kinetics. *Calphad: Computer Coupling of Phase Diagrams and Thermochemistry*, 72:102238, 2021. ISSN 03645916. doi: 10.1016/j.calphad.2020.102238.

[91] J. P. Best, Z. Evenson, F. Yang, A-C. Dippel, M. Stolpe, O. Gutowski, M. Tarik Hasib, X. Li, and J. J. Kruzic. Structural periodicity in laser additive manufactured Zr-based bulk metallic glass. *Applied Physics Letters*, 115(3):031902, 2019. ISSN 0003-6951. doi: 10.1063/1.5100050.

[92] J. Qiao, H. Jia, and P. K. Liaw. Metallic glass matrix composites. *Materials Science and Engineering R: Reports*, 100:1–69, 2016. ISSN 0927796X. doi: 10.1016/j.mser.2015.12.001.

[93] F. C. Li, T. Liu, J. Y. Zhang, S. Shuang, Q. Wang, A. D. Wang, J. G. Wang, and Y. Yang. Amorphous–nanocrystalline alloys: fabrication, properties, and applications. *Materials Today Advances*, 4, 2019. ISSN 25900498. doi: 10.1016/j.mtadv.2019.100027.

[94] F-F. Wu, K. C. Chan, S-S. Jiang, S-H. Chen, and G. Wang. Bulk metallic glass composite with good tensile ductility, high strength and large elastic strain limit. *Scientific reports*, 4:5302, 2014. ISSN 2045-2322. doi: 10.1038/srep05302.

[95] T. Gheiratmand and H. R. Madaah Hosseini. Finemet nanocrystalline soft magnetic alloy: Investigation of glass forming ability, crystallization mechanism, production techniques, magnetic softness and the effect of replacing the main constituents by other elements. *Journal of Magnetism and Magnetic Materials*, 408:177–192, 2016. ISSN 03048853. doi: 10.1016/j.jmmm.2016.02.057.

[96] J. Plocher and A. Panesar. Review on design and structural optimisation in additive manufacturing: Towards next-generation lightweight structures. *Materials and Design*, 183:108164, 2019. doi: 10.1016/j.matdes.2019.108164.

[97] A. Plotkowski, J. Pries, F. List, P. Nandwana, B. Stump, K. Carver, and R. R. Deho. Influence of scan pattern and geometry on the microstructure and soft- magnetic performance of additively manufactured Fe-Si. *Additive Manufacturing*, 29:100781, 2019. doi: 10.1016/j.addma.2019.100781.